Alma Mater Studiorum · Università di Bologna

Dipartimento di Fisica e Astronomia "Augusto Righi"
Corso di Laurea in Fisica

Search for Electroweak Supersymmetry in final states with a W boson and a Higgs boson with the ATLAS detector

Relatore:
Prof. Iacopo Vivarelli

Correlatore:
Dott. Eric Ballabene

Presentata da:
Silvia Vicentini

Anno Accademico 2024/2025

Abstract

Supersymmetry is one of the most promising extensions of the Standard Model, addressing several of its theoretical limitations and providing a natural dark matter candidate in the form of the lightest supersymmetric particle. Among the various Supersymmetry production mechanisms, the electroweak production of charginos and neutralinos is of particular interest due to its cleaner experimental signatures.

This work focuses on the simplified Supersymmetry process

$$pp \to \tilde{\chi}_1^{\pm}\tilde{\chi}_2^0 \to \tilde{\chi}_1^0\tilde{\chi}_1^0 Wh,$$

analysing final states with one or two charged leptons, using Monte Carlo simulations of events reconstructed by the ATLAS detector.

The goal of the analysis is to discriminate Supersymmetry signal from the SM backgrounds in different final states, taking into account the Standard Model branching ratios of the W and Higgs bosons. Signal regions are defined and optimized by studying the statistical significance in the single-lepton and dilepton channels.

The dilepton channel is explored for the first time in this context. Although the expected significance is lower than the single-lepton channel, due to the reduced branching ratio, newly defined signal regions allow for an improvement in sensitivity.

In the single-lepton channel, several analysis strategies were employed. A Variational Autoencoder was used to detect signal-like anomalies, demonstrating good performance in scenarios with large mass splitting. In addition, both Cut and Count and Deep Neural Network techniques were applied and compared. The strategy based on the Deep Neural Network showed the best performance, yielding improved sensitivity for benchmark mass hypotheses. For instance, statistical significances of

$$Z = 2.48 \quad \text{and} \quad Z = 1.79$$

were obtained for the $m(\tilde{\chi}_1^{\pm}/\tilde{\chi}_2^0, \tilde{\chi}_1^0)$ =(500, 250) GeV and (800, 0) GeV mass hypotheses, respectively.

The results highlight the potential of machine learning methods, particularly Deep Neural Networks, to enhance sensitivity in searches for supersymmetric particles produced through the electroweak interaction.

Contents

Introduction

The Standard Model (SM) provides a coherent and predictive framework that successfully describes three of the four fundamental interactions (electromagnetic, weak, and strong) and accounts for all known elementary particles. However, astrophysical observations, starting from the study of the Coma Cluster in the 1930s, have provided indirect evidence of a form of matter that does not interact electromagnetically, known as dark matter (DM). Current cosmological measurements estimate that dark matter constitutes about 27% of the universe's total energy density, while ordinary matter accounts for only about 5%.

Since the Standard Model does not provide any viable particle candidate to explain the nature of dark matter, any attempt to interpret this phenomenon within the framework of particle physics, under the assumption that dark matter is indeed of particle nature, and not the result of gravitational or astrophysical effects, requires an extension of the model. One of the most promising is Supersymmetry (SUSY), which postulates the existence of a superpartner for each known particle, with the same quantum numbers but differing in spin. In particular, the lightest supersymmetric particle (LSP), which is stable in many SUSY scenarios, represents a natural DM candidate. Among the possible LSPs, the neutralino $\tilde{\chi}_1^0$ is of particular interest in this thesis.

The ATLAS experiment, located at the Large Hadron Collider (LHC) at CERN, provides the opportunity to investigate the possible production of supersymmetric particles. This thesis focuses on the analysis of proton-proton collision events at centre-of-mass energies of $\sqrt{s} = 13$ TeV and $\sqrt{s} = 13.6$ TeV, which may lead to the production of neutralinos $\tilde{\chi}_2^0$ and charginos $\tilde{\chi}_1^{\pm}$. These particles subsequently decay into the neutralino $\tilde{\chi}_1^0$, a candidate LSP, and a W and a h bosons.

The goal of the analysis is to define selections (cuts) on kinematic variables in order to optimize the signal-to-background ratio, comparing two different approaches: the traditional Cut and Count (C&C) method and a machine learning technique based on Deep Neural Networks (DNNs). The study demonstrates the greater effectiveness of the DNN in discriminating signal from background.

The analysis is performed on final states with one and two leptons, and also includes the investigation of an unsupervised model, the Variational Autoencoder (VAE), for signal-background separation.

Chapter 1 introduces the SM and its main limitations, followed by the SUSY extension and the supersymmetric particles relevant to this analysis. Chapter 2 describes

the ATLAS detector and the main mechanisms for the reconstruction of physical objects. Finally, Chapter 3 presents the data analysis, detailing the methods employed and discussing the results obtained.

Chapter 1

Standard Model and Supersymmetry

The first step in the study of elementary particles was marked in 1897 by the discovery of the electron, which paved the way for understanding the structure of the atom and the nucleus. The subsequent exploration of atomic structure led to the identification of the proton and neutron. These subatomic particles, among the first to be discovered, constitute the stable matter of the universe. However, the observation of cosmic rays, jets of high-energy particles originating from outer space, revealed the existence of numerous additional particles, some akin to those already known and others of fundamentally different character. Over the course of the 20th century, thanks to increasingly sophisticated experiments, the SM was developed: a coherent, extensively validated theory that identifies the elementary particles comprising matter and delineates the fundamental interactions governing their behaviour.

This chapter presents the structure of the SM, examines its limitations, and demonstrates how supersymmetry provides consistent resolutions to these discrepancies.

1.1 The Standard Model

The study of elementary particles falls within the domain of quantum field theory (QFT), a framework that recasts quantum mechanics, the mechanics of microscopic bodies, within a relativistic setting, since the objects under consideration move at speeds approaching that of light [1]. In QFT, particles are interpreted as excitations of fields, each described through a Lagrangian formalism. Moreover, these Lagrangians must be invariant under the symmetry group

$$U(1) \times SU(2)_{\mathrm{L}} \times SU(3) \tag{1.1}$$

from which the SM is derived. From the symmetry associated with $U(1) \times SU(2)_{\mathrm{L}}$ electroweak interactions emerge. Likewise, from the symmetry under $SU(3)$ quantum chromodynamics (QCD) arises, which describes the strong interactions.

The SM classifies all known elementary particles into a compact set of fundamental constituents, as illustrated in Figure 1.1. These are grouped into two categories:

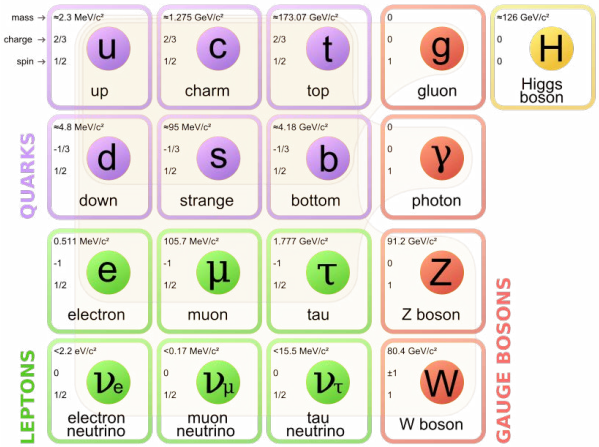

Figure 1.1: Schematic representation of the elementary particles comprising the SM.

fermions, which are half-integer spin particles obeying Fermi–Dirac statistics, and bosons, integer-spin particles following Bose–Einstein statistics. Moreover, each fermion has an associated antiparticle, identical in mass but with opposite electric charge.

Fermions are further subdivided into quarks and leptons. Quarks are arranged in three generations, each containing one positively charged quark with $q = +\frac{2}{3}$ and one negatively charged quark with $q = -\frac{1}{3}$: the up (u and down (d), charm (c) and strange (s), and finally top (t) and bottom/beauty (b) quarks. These generations are listed in order of increasing mass. Quarks participate in the strong, weak, and electromagnetic interactions. Notably, quarks are never observed isolated, but instead exist only in bound states known as hadrons, which can be mesons (comprising a quark–antiquark pair) or baryons (comprising three quarks). Protons and neutrons, for example, are the most familiar baryons and are composed of up and down quarks.

Leptons are organized into three generations of increasing mass: the electron (e), the muon (μ), and the tau (τ), each carrying one electric negative charge. Associated with each of these charged leptons is a corresponding neutrino of a specific flavour: the electron neutrino (ν_e), the muon neutrino (ν_μ), and the tau neutrino (ν_τ). Within the SM framework, neutrinos are assumed to be massless. Leptons interact only via the electromagnetic and weak forces, they do not participate in the strong interaction.

Among the bosons, a distinction is made for the mediators of the fundamental interactions, all of spin 1, also known as gauge bosons. The photon (γ) mediates the electromagnetic interaction, gluons (g) (eight in total) mediate the strong interaction, and the W^+ and W^- bosons mediate the weak interaction via charged currents, while the Z boson mediates the weak interaction via neutral currents. Among these, only the mediators of the weak interaction possess mass.

Finally, with zero spin, there is the Higgs boson (h). It is through interaction with this field that particles in the SM acquire mass.

1.1.1 The Higgs Mechanism

The Higgs boson was theorized in 1964. The idea from which this particle arises stems from the fact that the particles of the SM must be described, as previously mentioned, by Lagrangians invariant under local gauge transformations. To impose this condition, it is necessary that particles with spin zero or one-half interact with a vector field that is massless.

This leaves unexplained how weak interactions can be mediated by very massive bosons. Indeed, the mass of the W boson is $80.4\,\mathrm{GeV/c^2}$ [2] and the mass of the Z boson is $91.2\,\mathrm{GeV/c^2}$ [3]. To resolve this apparent contradiction, Higgs hypothesized the existence of a scalar field, known as the Higgs field, subject to the potential [4]

$$U(\phi) = -\frac{1}{2}\mu^2|\phi|^2 + \frac{1}{4}\lambda(|\phi|^2)^2 \tag{1.2}$$

depicted in Figure 1.2. This potential has two symmetric minima at $\phi = \pm\frac{\mu}{\lambda} \neq 0$. The system spontaneously evolves toward a potential minimum, thereby assuming a non-symmetric configuration and performing the so-called spontaneous symmetry breaking.

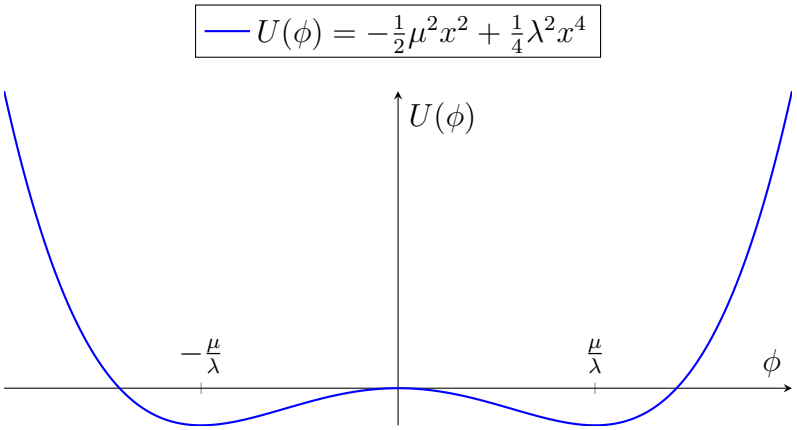

Figure 1.2: Illustration of the Higgs field potential $U(\phi)$, featuring its minima at $\phi = \pm\mu/\lambda$.

In this process, by imposing invariance of the Lagrangian under local gauge transformations, the vector field acquires mass. This process is known as the Higgs mechanism. It is therefore the interaction of these particles with the Higgs field that endows them with mass.

The Higgs boson was first observed in 2012 by the ATLAS and CMS collaborations at the LHC, with a mass of approximately $m_h = 125\,\mathrm{GeV}$ [5], thus confirming theoretical predictions.

1.2 Limits of the Standard Model

The SM, while remarkably successful in explaining the majority of phenomena in subnuclear physics, nonetheless leaves several unresolved questions. The most pertinent issues addressed in this thesis are [6, 7]:

- **The nature of dark matter.** Although it comprises approximately 27% of the matter in the universe, it has eluded direct detection by current instrumentation.
- **The mass of the Higgs boson.** Theoretically, its mass is expected to be much larger than the value experimentally observed.
- **The unification of fundamental interactions.** A coherent theoretical framework to unify the various forces described by the SM remains elusive.

In the following sections, each of these issues will be analysed in greater detail, and it will be shown how the SUSY framework offers potential resolutions.

1.3 Supersymmetry

The Emy Noether theorem asserts that every mathematical symmetry corresponds to a physical conservation law, and vice versa. This fundamental principle underpins the entirety of twentieth-century physics. It is on this basis that isospin doublets were theorized within the SM, for instance. In 1974, Wess and Zumino introduced a symmetry relating particles whose spins differ by one-half. For example, considering transformations for a scalar field ϕ and a spinor field ψ [7]

$$\phi \to \phi + \delta\phi = \phi + 2\bar{\epsilon}\psi \tag{1.3}$$

$$\psi \to \psi + \delta\psi = \psi - \left(\frac{i}{\hbar c}\right)\gamma^{\mu}\epsilon(\partial_{\mu}\phi) \tag{1.4}$$

where ϵ is a spinor describing the transformation and $\bar{\epsilon}$ is its adjoint. In order for the Lagrangian of a spin-zero particle (the Klein–Gordon Lagrangian) and that of a spinorial particle (the Dirac Lagrangian) to remain invariant under these transformations, it is necessary that the two fields possess the same mass. The same result is obtained when working with particles of spin $\frac{1}{2}$ and 1. This invariance thus connects fermions and bosons and is known as Supersymmetry. In addition to sharing the same mass, supersymmetric partners also carry identical electric charge, weak isospin, and colour degrees of freedom.

Particle	**Spin**	**Sparticle**	**Spin**
quark q	1/2	squark $\tilde{q}$	0
lepton l	1/2	slepton $\tilde{l}$	0
photon γ	1	photino $\tilde{\gamma}$	1/2
gluon g	1	gluino $\tilde{g}$	1/2
$W^{\pm}$	1	wino $\tilde{W}^{\pm}$	1/2
Z^0	1	zino $\tilde{Z}^0$	1/2
$(h_u^0\ h_u^+)$	0	$(\tilde{h}_u^0\ \tilde{h}_u^+)$	1/2
$(h_d^0\ h_d^-)$	0	$(\tilde{h}_d^0\ \tilde{h}_d^-)$	1/2

Table 1.1: SM particles and their supersymmetric partners in the MSSM.

The Minimal Supersymmetric SM (MSSM) [8] is the model that introduces the smallest possible number of additional particles required to realize a supersymmetric theory.

According to this framework, each fermion is assigned a supersymmetric partner denoted by the prefix s–, represented by the same symbol as the fermion but with a tilde above it. Conversely, the supersymmetric partners of bosons receive the suffix –ino. Finally, in a supersymmetric theory there are two Higgs doublets, each accompanied by their own supersymmetric partners. The components that constitute the MSSM are listed in Table 1.1.

The power of supersymmetry lies in its ability to address the three issues previously identified in the SM.

1.3.1 The Dark Matter

The SM describes only 5% of the mass and energy constituting the universe, with the remaining contribution given by approximately 27% dark matter and 68% dark energy. In 1933, Fritz Zwicky, a Swiss astronomer, measured the overall velocity of the Coma cluster from the Doppler shift effect observed in the spectra of the atoms composing the cluster. The value he obtained was surprisingly high: based on the visible mass composing the cluster, the galaxies would have been able to escape from their mutual gravitational field. For this reason, he hypothesized the existence of a type of high-density matter that does not emit radiation and therefore does not appear in the spectrum, hence the name dark matter.

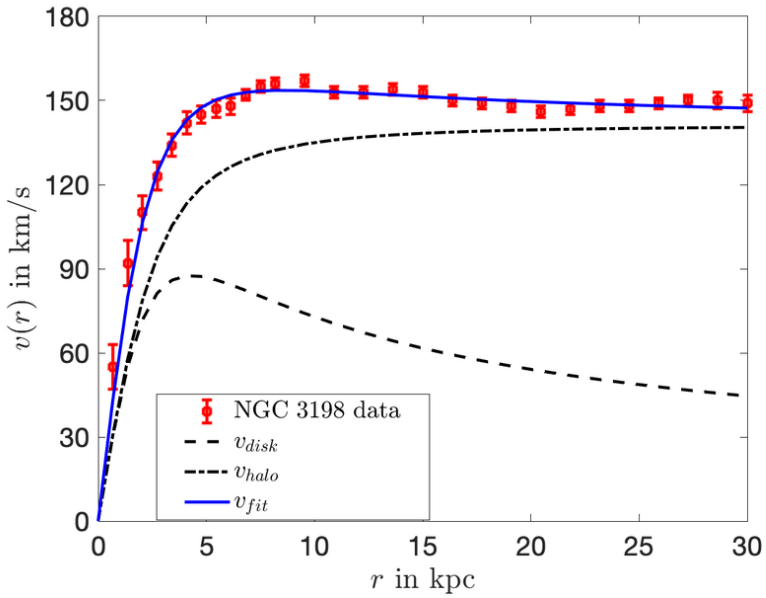

Figure 1.3: Rotation velocity of the galaxy NGC 3198 as a function of the distance from the galactic centre. The predicted trends according to the rotating disk model and dark matter halo are compared with experimental results [9].

Forty years later, Vera Rubin measured the rotation velocity of individual galaxies, obtaining results analogous to those of her colleague. Through classical calculations it is possible to estimate the velocity behaviour of an infinitesimal mass element dm as a function of the distance r from the galaxy centre, approximated as a disk of radius R

rotating about an axis passing through its centre. In this case, the expected behaviour is

$$v(r) \propto \begin{cases} r & \text{if } r < R \\ \frac{1}{\sqrt{r}} & \text{if } r > R \end{cases} \tag{1.5}$$

The result obtained by the astronomer underestimated the value of R beyond which a decrease in the galaxy's velocity should be observed. Moreover, the experimentally obtained velocity did not tend to zero, as shown in Figure 1.3. It is therefore evident that there must exist other matter of an unknown nature, that does not emit radiation.

Over the years, numerous additional experimental evidences have been collected supporting the existence of dark matter. Thanks to these, it can be asserted that dark matter must possess the following characteristics:

- it must be stable, since it has been present since the primordial epochs of the universe;
- it must not be affected by either the strong or electromagnetic interactions, otherwise it would be naturally produced in colliders, would interact with ordinary matter, and would emit visible radiation;
- it must be very massive, to explain the experimental results discussed.

The Standard Model does not include any particle with properties compatible with those required to explain dark matter. Among the proposed extensions of the Standard Model, a prominent hypothesis is the existence of Weakly Interacting Massive Particles (WIMPs), which provide a plausible candidate for dark matter. However, it should be noted that WIMPs represent only one of several possible solutions within the framework of particle physics.

Supersymmetry provides a suitable WIMP candidate to represent dark matter: the neutralino, whose lightest state is denoted as $\tilde{\chi}_1^0$. This particle is massive, neutral, and stable.

1.3.2 The Hierarchy Problem

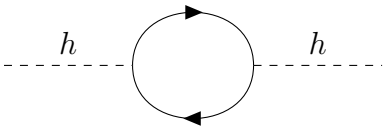

Figure 1.4: Higher-order Feynman diagram illustrating a Higgs field loop containing a fermion-antifermion pair.

The physical mass value of particles measured in laboratory experiments is given by the mass obtained from first-order perturbative Feynman diagrams, to which various corrections from higher-order Feynman diagrams, such as the one depicted in Figure 1.4, are added. In QFT it is found that for fermions and vector bosons these corrections depend on the centre-of-mass energy q as $\delta m \propto \ln(q^2)$. Being logarithmic, these corrections do

not significantly alter the theoretical mass value obtained from the leading order (LO) diagram.

However, for the Higgs boson, the correction is proportional to $\delta m \propto q^2$, a correction that rapidly increases the initial mass at high centre-of-mass energies. Theoretically, this results in an overestimation of the Higgs boson mass by several orders of magnitude compared to the experimentally measured value. This discrepancy between theoretical predictions and experimental results is known as the Hierarchy problem.

Working within the framework of SUSY theory, the loops that can form involve not only fermions but also their respective bosonic supersymmetric partners. The corrections arising from fermions are positive, while those from bosons are negative. Consequently, the mass derived at leading order remains essentially unchanged through the running of the parameters.

1.3.3 The Unification of Fundamental Interactions

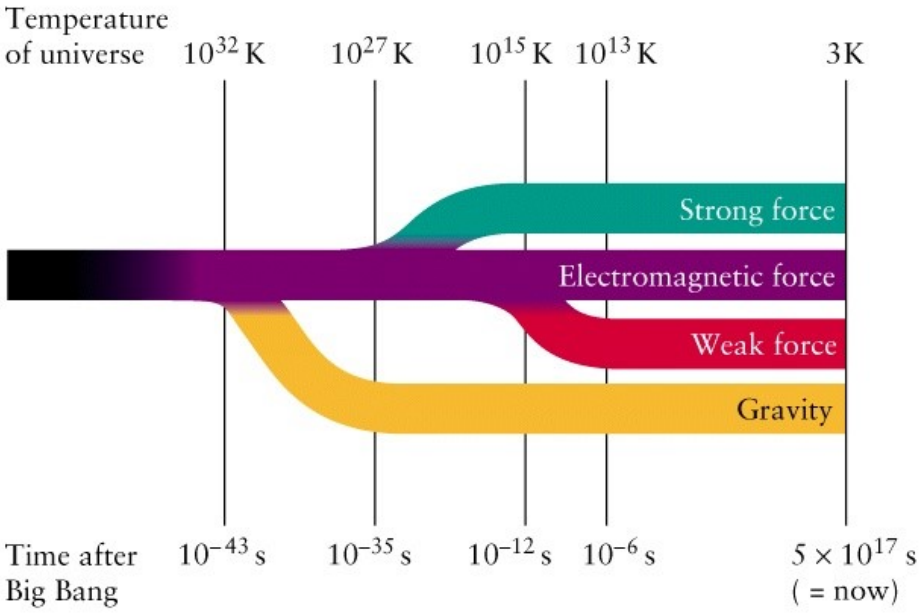

Figure 1.5: Eras of the universe's evolution from the Big Bang to the present day.

The universe originated from the Big Bang, when all matter and energy, concentrated in an infinitely small, hot, and dense point, suddenly began to expand. The history of the universe can be divided into four eras:

- during the Planck era, which ended 10^{-43} s after the Big Bang, it is hypothesized that the four fundamental interactions, gravitational, electromagnetic, strong, and weak, were unified.
- during the GUT era, which ended 10^{-35} s after the Big Bang, the gravitational interaction separated from the other three;
- during the inflationary era, which ended 10^{-32} s after the Big Bang, the universe underwent a rapid expansion during which the temperature dropped from $T =$

10^{-27} K to $T = 10^{-22}$ K. Under these conditions, the strong interaction separated from the electroweak interaction;

- during the electroweak era, which ended 10^{-12} s after the Big Bang, the electromagnetic and weak interactions separated. In this epoch, rapid expansion continued and the temperature decreased to approximately $T = 10^{-15}$ K;
- during the current era, from 10^{-12} s to 5×10^{17} s after the Big Bang, the four fundamental interactions are distinct and the average temperature of the universe is about $T = 3$ K.

Currently, each of the four fundamental interactions has a distinct coupling constant that defines the strength of the interaction. The strongest among the four is the strong interaction, with a coupling constant α_s which at low energies is approximately equal to 1. Next is the electromagnetic interaction, with a coupling constant $\alpha = \frac{1}{137} \approx 10^{-2}$. For the weak interaction, defining a single coupling constant is more complex; however, it can be stated that the interaction strength is proportional to the Fermi constant, $G_F \approx 10^{-5}\,\mathrm{GeV}^{-2}$. Finally, the gravitational interaction is the weakest of the four, being proportional to the universal gravitational constant, $G = 6.674 \times 10^{-11}\,\mathrm{m}^3\,\mathrm{kg}^{-1}\,\mathrm{s}^{-2}$.

Through the process of parameter running within the SM, it is possible to modify, besides particle masses, also the values of the coupling constants. However, at the energy scale of the GUT era, i.e., around 10^{15} GeV, these corrections do not lead to the same values for the coupling constants associated with the first three forces, contrary to expectations; therefore, the three forces cannot be unified.

Supersymmetry theory allows for modifying the running of the coupling constants according to the trends shown in Figure 1.6, so that under the energy conditions at the GUT scale, the three constants converge to the same value [10].

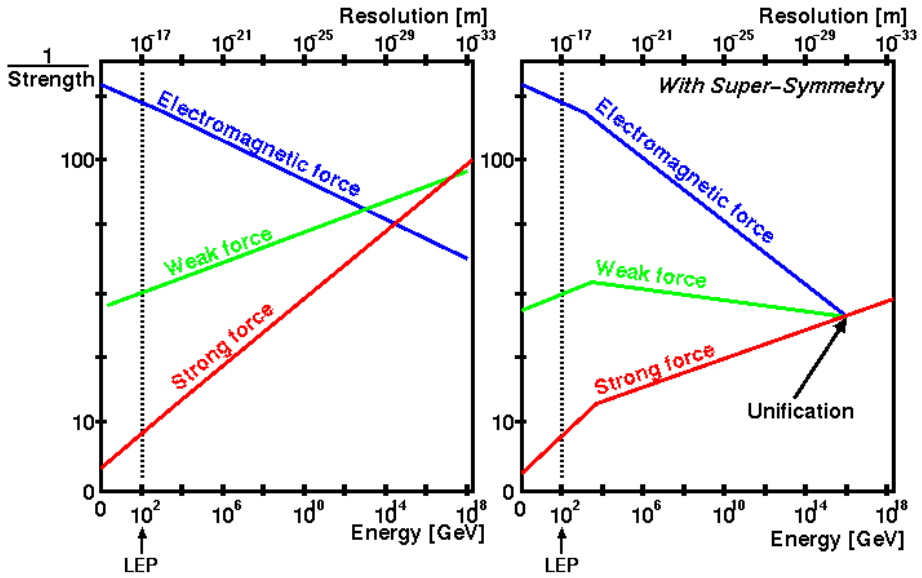

Figure 1.6: Running of the coupling constants of the strong interaction, the electromagnetic interaction and the weak interaction as a function of energy in the centre-of-mass reference frame according to the SM (left graph) and the MSSM (right graph).

1.4 Charginos and Neutralinos

According to electroweak theory, which unifies the electromagnetic and weak interactions, the bosons $W^{\pm}$, Z^0, and γ are linear combinations of the gauge bosons arising from the invariance of the SM Lagrangian under local gauge transformations. The $U(1)$ invariance gives rise to the vector boson B, while the $SU(2)$ invariance generates three vector bosons denoted as W^1, W^2, and W^3. These four bosons combine to form the mediators of the electromagnetic and weak interactions.

According to SUSY, each of these four gauge bosons has a supersymmetric partner: $\tilde{B}$, known as the bino, and $\tilde{W}^1$, $\tilde{W}^2$, and $\tilde{W}^3$, known as winos. The $\tilde{W}^3$ is often also denoted as $\tilde{W}^0$. The neutral gauge bosons $\tilde{B}$ and $\tilde{W}^0$ mix with the two neutral higgsinos, $\tilde{h}_u^0$ and $\tilde{h}_d^0$, to form four neutralinos, denoted as $\tilde{\chi}_i^0$ with $i = 1, 2, 3, 4$. Their masses can be derived from the mass matrix [10]

$$M_{\tilde{\chi}^0} = \begin{pmatrix} M_1 & 0 & -M_Z c_\beta s_{\theta_W} & M_Z s_\beta s_{\theta_W} \\ 0 & M_2 & M_Z c_\beta c_{\theta_W} & -M_Z s_\beta c_{\theta_W} \\ -M_Z c_\beta s_{\theta_W} & M_Z c_\beta c_{\theta_W} & 0 & -\mu \\ M_Z s_\beta s_{\theta_W} & -M_Z s_\beta c_{\theta_W} & -\mu & 0 \end{pmatrix} \tag{1.6}$$

where:

- M_1 and M_2 are the masses of the bino and wino gauginos;
- M_Z is the mass of the Z boson;
- μ is the higgsino mass parameter;
- θ_W is the Weinberg angle (approximately 29°);
- β is the higgsino mixing angle, defined through the relation $\tan(\beta) = \frac{v_u}{v_d}$, where v_u and v_d are the vacuum expectation values of the fields $\tilde{h}_u^0$ and $\tilde{h}_d^0$, respectively;
- c_θ and s_θ represent the trigonometrical functions $\sin\theta$ and $\cos\theta$.

Diagonalizing this matrix yields the masses of the four neutralinos.

From the linear combination of the charged winos and higgsinos, $\tilde{W}^{\pm}$, $\tilde{h}_u^+$, and $\tilde{h}_d^-$, one obtains the two charginos, denoted as $\tilde{\chi}_i^{\pm}$ with $i = 1, 2$. Their masses can be derived by diagonalizing the corresponding mass matrix

$$M_{\tilde{\chi}^{\pm}} = \begin{pmatrix} M_2 & \sqrt{2} M_W s_\beta \\ \sqrt{2} M_W c_\beta & \mu \end{pmatrix} \tag{1.7}$$

The masses appearing in the mass matrices are free parameters of the theory. There are three main scenarios related to the values of these parameters, which significantly influence the kinematics of supersymmetric processes, as shown in Figure 1.7.

When $\mu \gg M_2 > M_1$, one obtains the so-called wino–bino hierarchy. Under these conditions, the chargino $\tilde{\chi}_1^{\pm}$ and the neutralino $\tilde{\chi}_2^0$ are nearly mass-degenerate and almost pure wino eigenstates, heavier than the lightest neutralino $\tilde{\chi}_1^0$, which is almost a pure bino state and serves as the LSP.

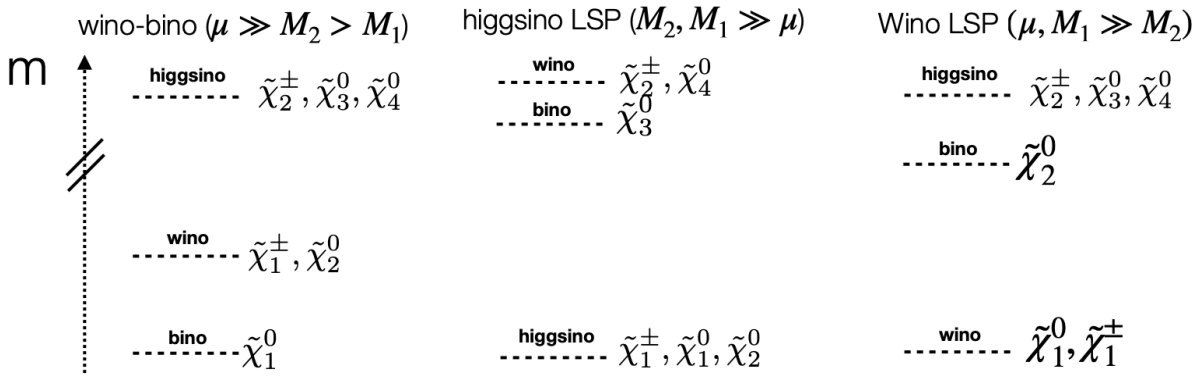

Figure 1.7: Representation of three of the most studied mass hierarchies of the MSSM model.

Their mass is given by

$$m_{\tilde{\chi}_1^0} = M_1 - \frac{M_Z^2 s_{\theta_W}^2 (M_1 + \mu \sin 2\beta)}{\mu^2 + M_1^2} + ..., \tag{1.8}$$

$$m_{\tilde{\chi}_2^0} = M_2 - \frac{M_{\theta_W}^2 (M_2 + \mu \sin 2\beta)}{\mu^2 + M_2^2} + ..., \tag{1.9}$$

$$m_{\tilde{\chi}_1^{\pm}} = M_2 - \frac{M_W^2 (M_2 + \mu \sin 2\beta)}{\mu^2 M_2^2} + ..., \tag{1.10}$$

In this scenario, the typical decays are

$$\tilde{\chi}_2^0 \to \tilde{\chi}_1^0 Z,\ \tilde{\chi}_1^{\mp} W^{\pm},\ \tilde{\chi}_1^0 h,\ \tilde{l}l,\ \tilde{\nu}\nu \tag{1.11}$$

$$\tilde{\chi}_1^{\pm} \to \tilde{\chi}_1^0 W^{\pm},\ \tilde{\chi}_1^{\pm} Z,\ \tilde{\chi}_1^0 h,\ \tilde{\nu}l,\ \tilde{l}\nu. \tag{1.12}$$

This is the setting on which the analysis performed in this thesis are focused.

Chapter 2

LHC and the ATLAS Detector

Nowadays, experimental research in particle physics is conducted at particle accelerators, devices capable of bringing particle beams to extremely high energies and colliding them in order to study the physical phenomena that arise from such interactions.

This chapter presents the main features of the LHC, currently the most powerful accelerator in the world, and provides a detailed description of the ATLAS experiment. The operating principles of its subdetectors and the detection techniques used to track and identify the particles produced in the collisions will also be illustrated.

2.1 The Large Hadron Collider

The LHC is the largest and most powerful particle accelerator in the world, designed by the European Organization for Nuclear Research (Conseil Européen pour la Recherche Nucléaire, CERN). It is used to study collisions between hadrons, either protons or heavy ions. It is located in a circular tunnel with a circumference of approximately 27 km, at an average depth of 100 m beneath the border between Switzerland and France, near Geneva. Originally commissioned in 1988 to host the Large Electron-Positron Collider (LEP), the tunnel was adapted between 2000 and 2008 to accommodate the LHC. Currently, the accelerator can reach centre-of-mass energies of up to $\sqrt{s}$ =13.6 TeV.

The decision to replace LEP with the LHC is motivated by the behaviour of electric charges when accelerated or decelerated. Synchrotron radiation, which results from accelerating electric charges along a circular path, as occurs in colliders, is proportional to

$$\frac{\mathrm{d}E}{\mathrm{d}t} \propto \frac{E^4}{m^4} \tag{2.1}$$

Therefore, the lower the mass of the accelerated particle, the greater the energy loss due to radiation. In fact, the maximum centre-of-mass energy reached at LEP was limited to 209 GeV, mainly due to the relatively low mass of the electrons compared to that of protons. While electron collisions allow for a cleaner environment and the possibility of probing higher energy processes, proton collisions enable exploration of a broader range of phenomena, albeit with more complex backgrounds due to QCD processes, since protons are not elementary particles.

At the LHC, two proton beams circulate in opposite directions. Each beam is composed of bunches of protons, each consisting of approximately 10^{11} particles, confined within transverse dimensions on the order of tens of μm. The event rate for a given process can be estimated using the relation

$$\frac{\mathrm{d}N}{\mathrm{d}t} = \sigma L, \tag{2.2}$$

where σ is the cross section of the process and L is the instantaneous luminosity, defined as

$$L = \frac{n_+ n_- f}{4\pi\sigma_x\sigma_y} n_b, \tag{2.3}$$

where:

- n_+ and n_- are the number of particles in the colliding bunches;
- f is the bunch crossing frequency;
- σ_x and σ_y are the transverse dimensions of the bunches;
- n_b is the number of circulating bunches.

It is therefore essential to maximize the value of L in order to increase the number of observable events for the processes under study. This number is given by

$$N(t_2, t_1) = \sigma \int_{t_1}^{t_2} L \,\mathrm{d}t = \sigma\mathcal{L}. \tag{2.4}$$

Here $\mathcal{L}$ represents the integrated luminosity. It is measured in fb^{-1}, where one barn is equivalent to $1\ \mathrm{b} = 10^{-24}\,\mathrm{cm}^2$.

Table 2.1 summarizes the values of beam energy and intedrated luminosity achieved during the data-taking periods of ATLAS, known as Runs, between 2015 and 2025. This thesis focuses on the data collected during Run 2 and Run 3.

Run Period	$\sqrt{s}$ (TeV)	$\mathcal{L}$ (fb^{-1})
Run 2 (2015–2018)	13	139.0
Run 3 (2022)	13.6	51.5
Run 3 (2024)	13.6	109.4
Run 3 (2025–2026)	13.6	-

Table 2.1: Summary of centre-of-mass energies and peak luminosities achieved during the LHC's main operational periods [11].

2.1.1 Proton Acceleration Process and Experiments at the LHC

The LHC is a synchrotron, a type of particle accelerator in which charged particles are propelled along circular trajectories. This is achieved using strong magnetic fields to bend their paths and oscillating electric fields to increase their energy. However, the acceleration of protons is not solely achieved within the LHC itself. The proton

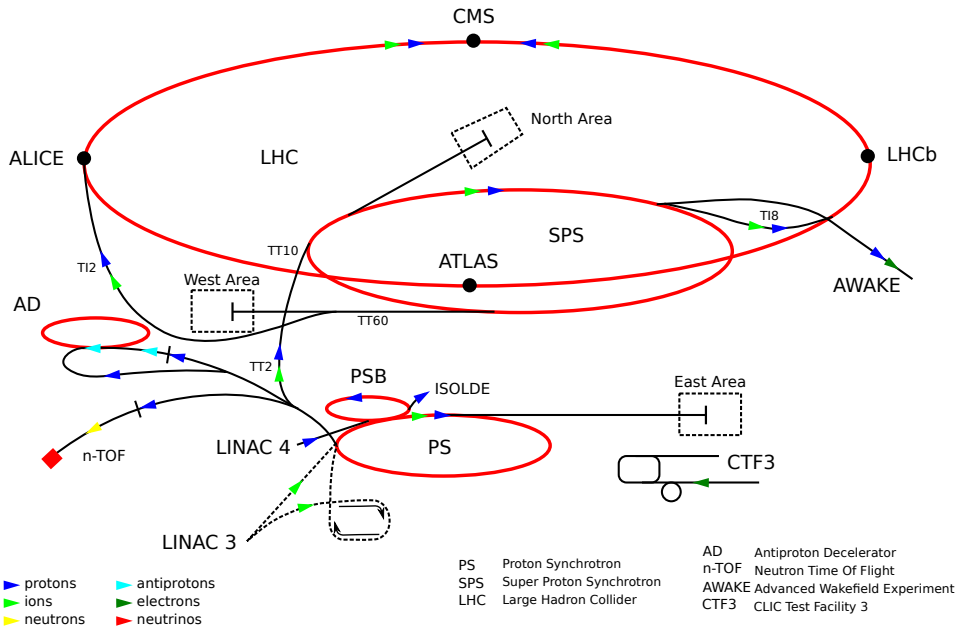

Figure 2.1: The CERN accelerator complex.

acceleration process involves several stages using a chain of accelerators preceding the LHC, as illustrated in Figure 2.1.

Protons are produced by ionizing a hydrogen source and are first accelerated to an energy of 160 MeV by LINAC4, a linear accelerator. They are then injected into the Proton Synchrotron Booster (PSB), a circular accelerator, where they reach an energy of 2 GeV. Subsequently, they enter the Proton Synchrotron (PS), which accelerates them up to 26 GeV. The protons are then transferred to the Super Proton Synchrotron (SPS), where they are accelerated to 450 GeV, and finally injected into the LHC, where the total energy at the collision point is equal to 13.6 TeV.

At the LHC, an oscillating electric field generated in the radiofrequency (RF) cavities is applied, synchronized with the passage of particle bunches along the beam. The frequency of this field is $f = \frac{n}{T}$, where T is the revolution period of the beam and n is an integer number. Thanks to this synchronization, the particles always encounter an accelerating electric field each time they pass through the RF cavities, allowing them to steadily increase their energy along the circular path.

To achieve stable circular orbits, the LHC relies on a powerful magnetic system. The LHC consists of 1232 dipole magnets with a magnetic field strength of 8.3 T, each approximately 15 m long and maintained at a temperature of 1.9 K, which serve to bend the trajectories of the beams into circular orbits. Additionally, it includes 392 quadrupole magnets, which are used to focus and collimate the beams.

Located along the LHC tunnel are four major experiments, positioned at the beam collision points, as shown in Figure 2.1. These experiments are:

- **ATLAS** (A Toroidal LHC Apparatus) [12] and **CMS** (Compact Muon Solenoid) [13], sharing the same scientific goals although the detectors are based on different

technologies, are designed to study the properties of the Higgs boson and to search for new physics beyond the SM.

- **ALICE** (A Large Ion Collider Experiment) [14] is dedicated to studying heavy-ion collisions in order to investigate the properties of the quark-gluon plasma.
- **LHCb** (Large Hadron Collider beauty experiment) [15] focuses on the study of hadrons containing beauty and charm quarks, with the aim of investigating the mechanisms responsible for matter-antimatter asymmetry.

2.2 The ATLAS Detector

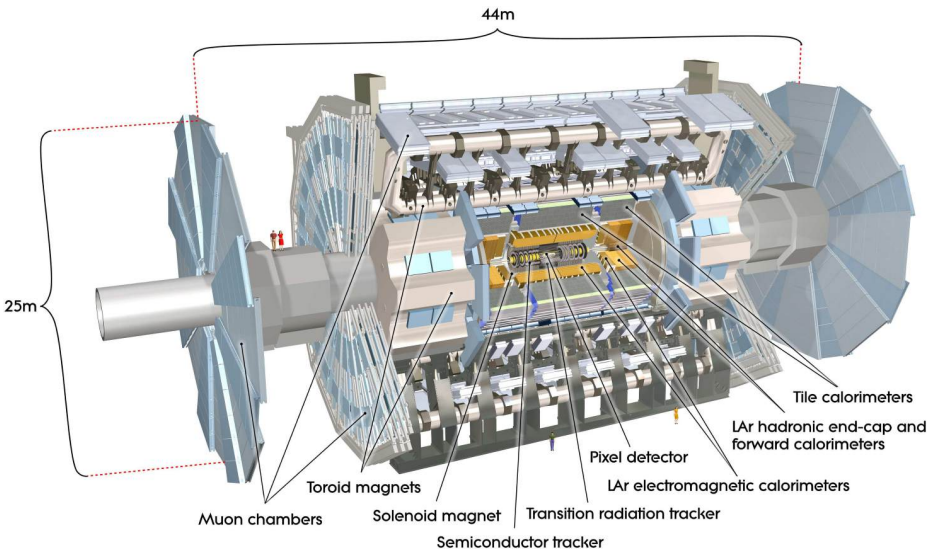

Figure 2.2: Structure of the ATLAS detector.

The ATLAS detector is located at the first proton–proton interaction point, approximately 100 m underground. It is 44 m long, has a diameter of 25 m, and weighs around 7000 tonnes.

The detector has cylindrical symmetry along the beam axis, which makes it convenient to describe it using a cylindrical coordinate system (z, ϕ, η). The origin of the coordinate system is set at the interaction point, at the centre of ATLAS. The z coordinate represents the distance along the beam axis from the origin. The azimuthal angle ϕ lies in the plane perpendicular to the z-axis. Instead of using the polar angle θ, the pseudorapidity is used, defined as

$$\eta = -\ln\left(\tan\frac{\theta}{2}\right). \tag{2.5}$$

It follows that $\eta = 0$ corresponds to the plane transverse to the beam direction, while $\eta \to \infty$ corresponds to the direction parallel to the beam. Distances in the (η, ϕ) plane

are parametrized as

$$R = \sqrt{(\Delta\phi)^2 + (\Delta\eta)^2}. \tag{2.6}$$

Each individual collision produces a large number of particles. For this reason, the detector must provide nearly full solid-angle coverage and be capable of rapid readout, in order to track all resulting events. To identify the wide variety of particles produced, the detector consists of several concentric subsystems, each designed to detect different types of particles. Starting from the innermost part, the main components are: the Inner Detector, the electromagnetic and hadronic calorimeters, and the Muon Spectrometer.

2.2.1 Magnet System

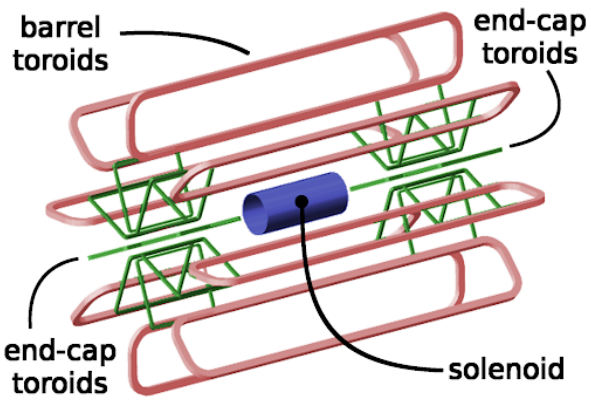

Figure 2.3: Magnet system of the ATLAS detector.

The ATLAS detector includes three magnet systems, as shown in Figure 2.3, which are maintained at cryogenic temperatures by a liquid helium cooling system. The magnets allow the bending of charged particles produced in the collisions, enabling the measurement of their transverse momentum according to the relation

$$p_{\mathrm{T}} = q|\vec{B}|\rho. \tag{2.7}$$

Located outside the Inner Detector is the Central Solenoid, which generates a magnetic field of 2 T. It has a radius of approximately 1.2 m, a length of 5.3 m, and is aligned parallel to the beam axis. It is used to curve the trajectories of all charged particles and to measure their transverse momentum.

The Barrel Toroid consists of eight rectangular coils arranged in a petal-like geometry around the z-axis. It is 25 m long and has an outer diameter of 20.1 m. It produces a magnetic field of 4 T, which is used to measure the curvature of muons, the only charged particles capable of passing through the calorimeters, in the central region of the detector, corresponding to $|\eta| < 1$.

The End-Cap Toroid is also composed of rectangular coils arranged with cylindrical symmetry; however, in this case, they are split into two sets of eight coils, one for each end-cap region, covering the forward and backward areas of the detector for $1 < \eta < 1.4$. Its inner diameter is approximately 1.6 m and the outer diameter is 10.7 m. The system

is designed such that the magnetic field it generates, reaching a maximum of 4 T, is orthogonal to the beam pipe, providing tracking information for muons produced at high pseudorapidity, close to the z-axis.

To summarize, the central solenoid acts on all charged particles. The toroids, on the other hand, act only on muons, which are the only charged particles capable of reaching the muon spectrometer. The three magnetic fields are independent from one another.

2.2.2 The Inner Detector

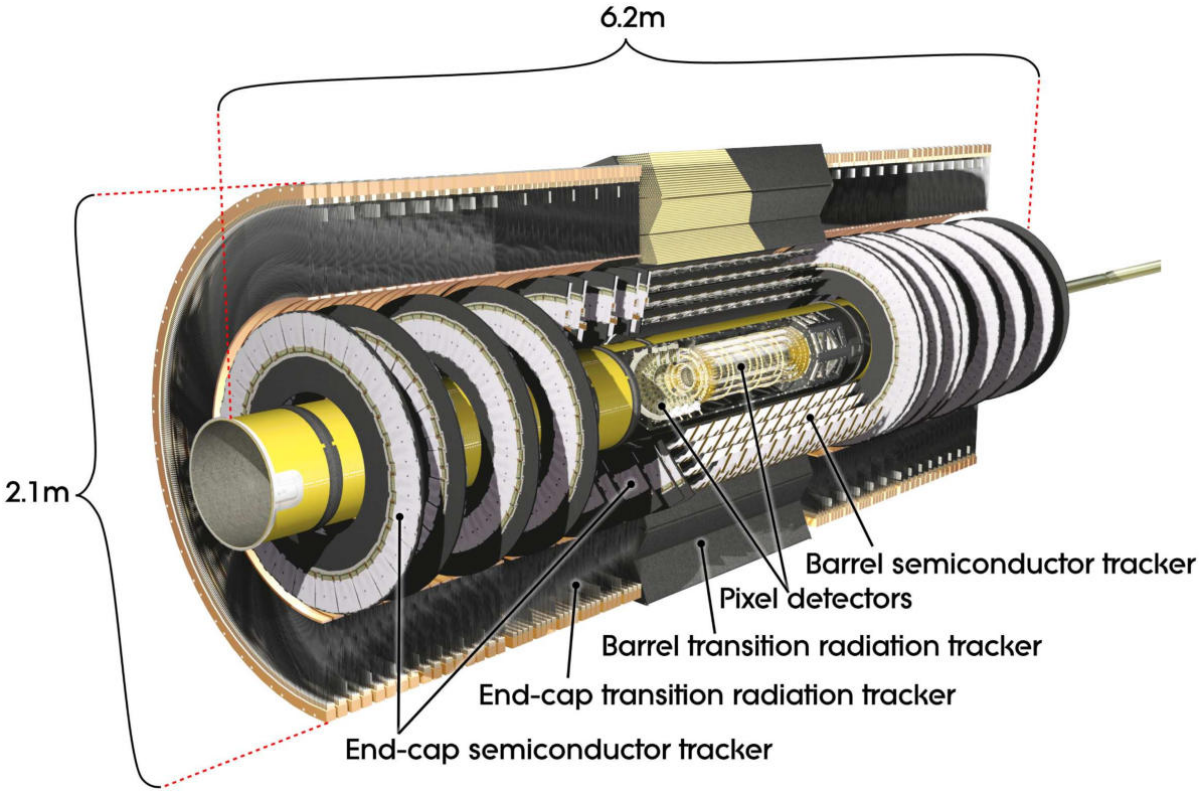

Figure 2.4: Structure of the Inner Detector.

The Inner Detector, shown in Figures 2.4 and 2.5, is the innermost detector and covers a region up to $\eta < 2.5$. Its purpose is to measure the charge, trajectory, and transverse momentum of particles produced at the primary and secondary vertices. Being the innermost system, it must be highly radiation-resistant. It consists of three subsystems: the Pixel Detector, the SemiConductor Tracker (SCT), and the Transition Radiation Tracker (TRT).

The Pixel Detector is the first layer of the Inner Detector, located between 33.25 mm and 122.5 mm from the beam line. It contains 87.2 million pixels of size 50×400 μm^2, for a total of 1744 silicon pixel sensors arranged in three layers. The innermost part is the Insertable B-Layer (IBL), a crucial component for identifying secondary vertices associated with the decay of baryons containing bottom quarks. As charged particles pass through the silicon modules, they generate electron-hole pairs in proportion to the particle's energy. A bias voltage is applied to separate these pairs and register the track

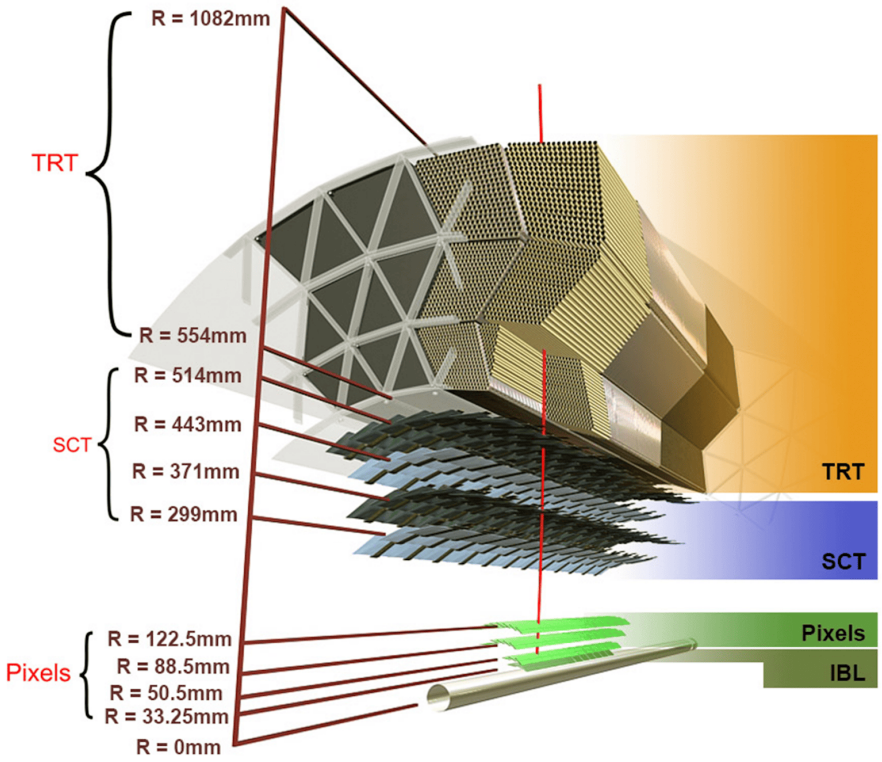

Figure 2.5: Transverse section of the Inner Detector.

of the incident particle. As the innermost detector, it is the most exposed to radiation and requires the most maintenance.

The SemiConductor Tracker (SCT) is located just outside the Pixel Detector and is composed of 4088 modules, arranged in four barrel layers in the central region of the detector ($|\eta| < 1.4$) and nine disks on each end-cap, covering the region $1.4 < |\eta| < 2.5$. On average, a charged particle traverses three measurements from the Pixel Detector and eight additional measurements from the SCT.

The Transition Radiation Tracker (TRT) is the outermost layer of the Inner Detector and is made of straw detectors — cylinders with a diameter of 4 mm, filled with a gas mixture mainly composed of xenon and carbon dioxide. When charged particles pass through the TRT, they emit transition radiation in the form of X-rays and also leave a trail of ionization electrons. Since the intensity of transition radiation is proportional to the Lorentz factor $\gamma = \frac{E}{m}$, combining this information with the energy measurements from the inner layers provides an initial method for particle identification. Nearly 400,000 straws are present, arranged in 73 layers parallel to the beam axis and 122 layers on each end-cap, oriented radially.

2.2.3 Calorimeters

Outside the Inner Detector lies the calorimeter system, which includes an electromagnetic calorimeter (ECAL) and a hadronic calorimeter (HCAL), as shown in Figure 2.6.

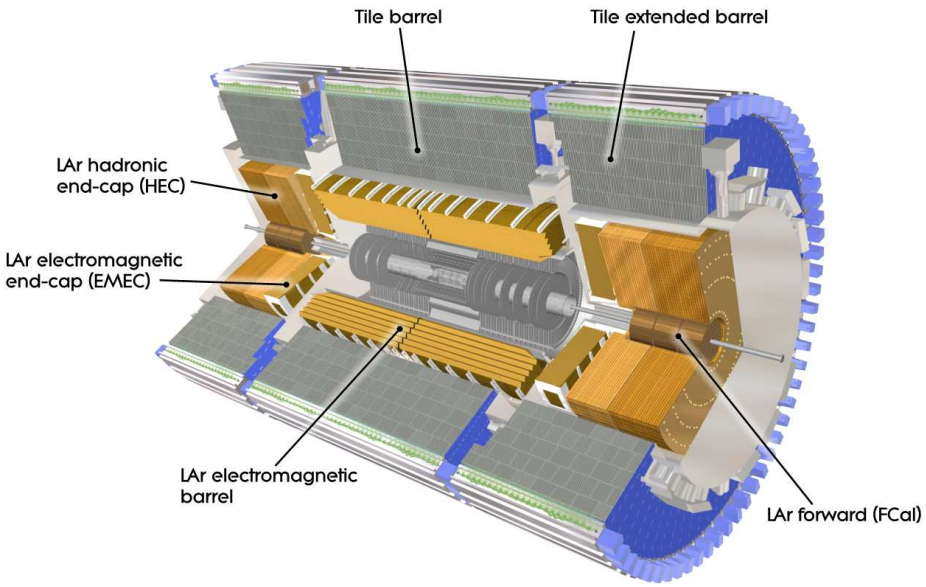

Figure 2.6: Section of the calorimeter system in ATLAS.

These are sampling calorimeters, composed of alternating layers of high-density passive material, which has a high probability of absorbing incident particles, and active material, which detects the passage of particles. They are used to measure the energy of electrons, photons, and hadrons produced in collisions. When these particles interact with matter, they produce a cascade of secondary particles known as a shower. Due to the different nature of photons and electrons compared to hadrons, the former interact electromagnetically, while the latter also undergo strong interactions, they produce very different showers, which are studied by separate calorimeters. From the shape and extension of these showers, the energy of the initial particles can be reconstructed. Electrons and photons are fully detected end measured by the electromagnetic calorimeters, whereas hadrons, passing through this first detector layer, lose only about 60% of their energy. Therefore, the remainder of the hadronic shower develops in the hadronic calorimeter, which measures the remaining approximately 40% of the energy.

The Electromagnetic Calorimeter (ECAL) consists of four sampling calorimeters that use liquid argon as the active medium and lead as the absorber material. For this reason, it is also referred to as the Liquid Argon Calorimeter (LAr). The ECAL has an accordion-shaped geometry, allowing for full coverage of the solid angle around the detector. The barrel section (EMB) covers the region $|\eta| < 1.475$, while the electromagnetic end-caps (EMEC) cover the range $1.375 < |\eta| < 3.2$.

The Hadronic Calorimeter (HCAL) is divided into two types of sampling calorimeters with different compositions: the Tile Calorimeter (TileCal) and the Hadronic End-Caps (HEC). TileCal uses scintillators as the active material and steel as the absorber. It consists of a Long Barrel (LB) that covers the region $|\eta| < 1$, and two Extended Barrels (EB) covering $0.8 < |\eta| < 1.7$. These are separated by a gap filled with scintillators to prevent energy loss in this area.

2.2.4 Muon Spectrometer

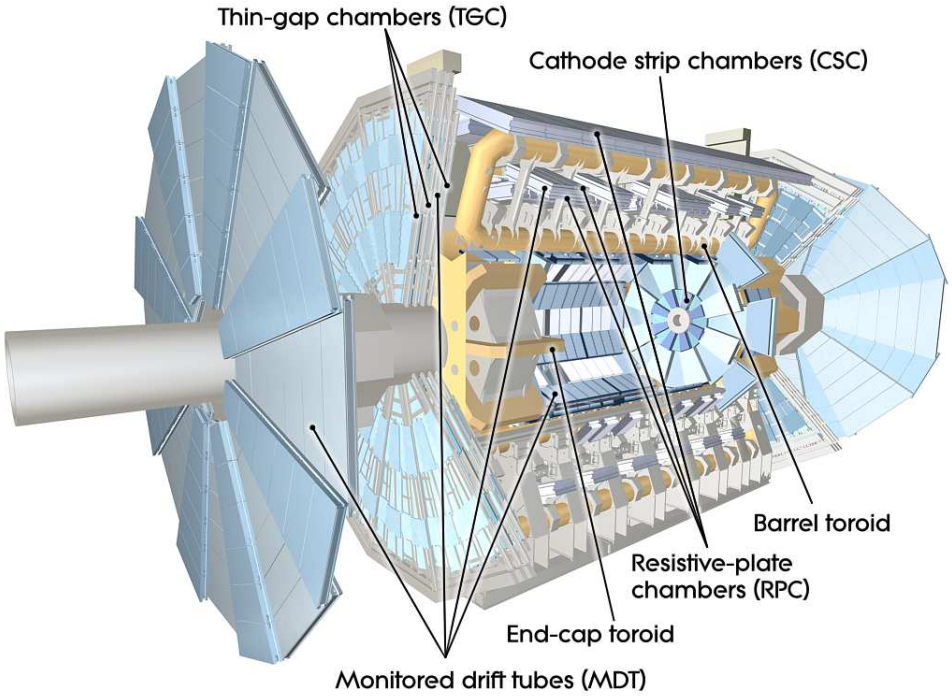

Figure 2.7: Structure of the Muon Spectrometer.

The only charged particles able to traverse the calorimeters are muons, due to their high mass and weak interaction with matter. These particles reach the Muon Spectrometer (MS), whose purpose is to precisely reconstruct their transverse momentum by exploiting the curvature of their trajectory in the magnetic field. In the barrel region, precision measurements are provided by Monitored Drift Tubes (MDTs), arranged in three cylindrical layers. Trigger information in the barrel is provided by Resistive Plate Chambers (RPCs). In the end-cap regions, muons are detected by the New Small Wheels (NSWs), which integrate two types of detectors: Micromegas (MM) and small-strip Thin Gap Chambers (sTGC), ensuring both precision tracking and fast triggering. Outside the NSWs, additional Thin Gap Chambers (TGCs) are used for triggering in the forward regions.

2.2.5 Trigger System

Experiments like ATLAS generate an enormous amount of data, on the order of 10^9 collisions per second, corresponding to approximately 1 PB of data per second. Therefore, it is essential to decide in real time which events to record for detailed analysis, reducing the data stream to manageable levels. The ATLAS trigger system [16] is designed to quickly select events of scientific interest from all those produced in collisions, while discarding less significant ones. This system operates in two main stages.

The first stage is the Level-1 trigger (L1), a hardware-based system that rapidly selects events using information from the calorimeters and the muon spectrometer. The decision to record an event is made in less than 2.5 µs.

The second-level trigger, known as the High-Level Trigger (HLT), is a software-based system that performs more complex analyses using a network of approximately 40,000 CPUs. This level refines the analysis of events selected by the L1 trigger, examining data from specific regions of the detector to determine which events are worth recording for detailed offline analysis.

2.3 Object Reconstruction

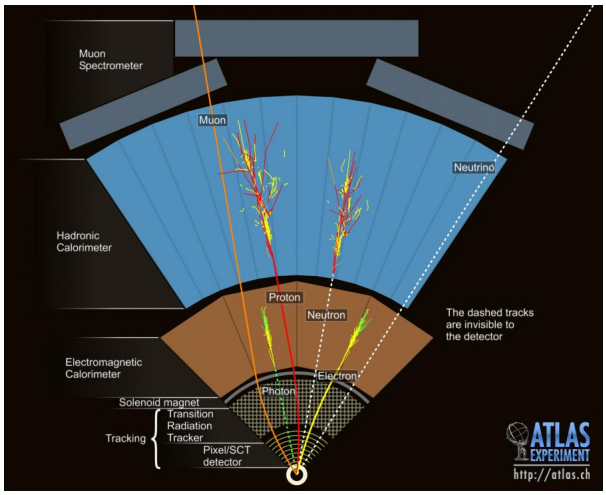

Figure 2.8: Section of the transverse plane in ATLAS. The figure illustrates the operating principle of the device used to distinguish the different particles produced in a given event.

The ATLAS detector collects a set of signals from which the physical processes must be reconstructed. The Inner Detector provides information in the form of charged particle tracks, the calorimeters measure electromagnetic and hadronic showers, and the muon spectrometer detects the passage of muons, as illustrated in Figure 2.8. Moreover, by combining the energies measured in the various subdetectors, the missing transverse energy, $E_{\mathrm{T}}^{\mathrm{miss}}$, can be inferred. Although these signals represent the only clues available to reconstruct the underlying physics event, they are not free from ambiguities. For this reason, various reconstruction algorithms are employed to deduce the most likely physical process from the measured data.

2.3.1 Electrons, Positrons and Photons

The identification of electrons and photons is performed through the ECAL, where the formation of electromagnetic showers is observed. These showers are initiated because high-energy electrons, being much lighter than hadrons, interact with matter primarily via Bremsstrahlung, the process consisting in emission of photons. In the case of photons, the dominant interaction mechanism is pair production, during which an e^+e^- pair is generated.

If the energy of the parent particle is sufficiently high, a cascade process is triggered: an electron emits a photon while losing energy, and the resulting photon in turn produces a new e^+e^- pair. Each of these particles continues to radiate in the same manner. The

initial energy is thus progressively distributed among the produced particles until the system reaches the critical energy E_C, at which point the aforementioned processes cease. A schematic representation of an electromagnetic shower is shown in Figure 2.9.

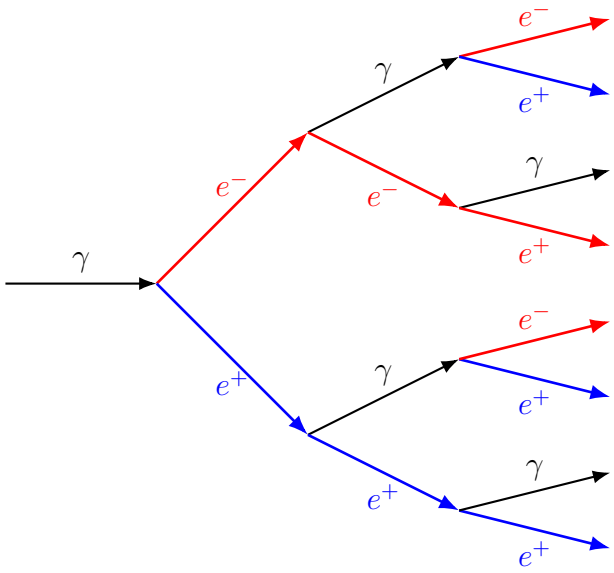

Figure 2.9: Representation of an electromagnetic shower generated by an high-energy photon.

To determine whether the parent particle is charged, such as an electron or a positron, or neutral, like a photon, its trajectory is analysed within the Inner Detector. As described by equation (2.7), charged particles interact with the magnetic field, resulting in a curved and well-defined trajectory. This trajectory can be reconstructed by the tracking detectors. In contrast, neutral particles do not produce a measurable track. Instead, they are identified indirectly through their energy deposits in the calorimeters. Further details on the reconstruction and identification of charged and neutral particles can be found in [17].

2.3.2 Muons

Muons can be distinguished from other charged particles because they are among the few capable of penetrating through the calorimeters and reaching the muon spectrometer, due to their minimal interaction with matter. Their transverse momentum is measured independently by both the Inner Detector and the muon spectrometer, as each system operates with a distinct magnetic field. By analysing the curvature of their trajectory, it is possible to determine both the charge of the particle and the energy it carries, as described by equation 2.7. For additional discussion, refer to [18].

2.3.3 Jets

The first objects to be identified in the event reconstruction are jets. According to the running of the coupling constants, the strong interaction coupling increases with the distance between interacting particles. This behaviour leads to the phenomenon

known as confinement, whereby quarks are never observed in isolation but are instead bound into colour-neutral states, primarily mesons and baryons. This process, known as hadronization [19], ensures that any free quark-antiquark pair produced in a high-energy proton-proton collision will give rise to a cascade of hadrons. In the centre-of-mass frame, the quark and antiquark move apart, and once the system's energy exceeds the threshold of $2m_q$, each of them, interacting with the quantum vacuum, radiates gluons. These gluons can generate new $q\bar{q}$ pairs, which subsequently hadronize. This results in the formation of numerous hadrons, mostly pions, π, that follow the direction of the original quark. An exception to this behaviour is the top quark, which, due to its extremely short lifetime, approximately 5×10^{-25} s, decays before it can hadronize and can thus be observed as a bare quark.

Jets are identified through electromagnetic and hadronic calorimeters, where hadronic showers are formed. By combining the trajectories of charged particles reconstructed in the Inner Detector with the energy deposits observed in the calorimeter, it is possible to infer the flavour of the originating quark. The hadronic shower also provides an estimate of the jet's total transverse energy.

Jet analysis is crucial to identify neutralinos and charginos, which is the purpose of this thesis. A key indicator of their possible presence is the missing transverse energy, $E_{\mathrm{T}}^{\mathrm{miss}}$, which signals an imbalance of energy in the plane transverse to the beam axis. Since the initial transverse momentum in a proton-proton collision is null, given that the protons move along the z-axis, momentum conservation dictates that the sum of the final transverse momenta should also be zero. If a non-zero transverse momentum vector is observed, its negative can be interpreted as a signature of neutral, undetected particles such as those predicted by SUSY. In order to observe such an imbalance, the reconstructed particles must carry high transverse momentum. Jets, being the result of quark and gluon fragmentation, typically carry large p_T and are thus essential for selecting events of interest.

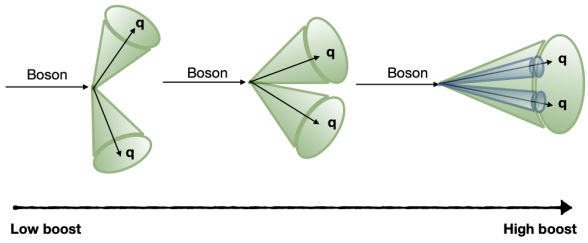

Figure 2.10: Spatial separation of two jets as a function of the energy involved, illustrating the transition to a boosted jet configuration.

When a heavy particle, such as a W or Z boson, is produced with high energy, its decay products, often a $q\bar{q}$ pair, are extremely collimated, meaning the resulting jets are emitted with a very small angular separation. In such cases, the jets appear to overlap and are better treated as a single, wide, and energetic jet, referred to as a boosted jet or a large-R jet, illustrated in Figure 2.10. Boosted jets are identified by the condition $R = 1.0$ while resolved jets by $R = 0.4$, where R [20] is defined in Equation 2.6.

A jet of particular interest in this analysis is the so-called b-jet, namely a jet originating

from the hadronization of a bottom quark. b-quarks have long lifetime, high mass, high decay multiplicity and a typical lifetime of the order of $\tau \approx 1.5$ ps. These properties are explored by *b-tagging* algorithms to identify b-jets with high efficiency. In this thesis, the GN2 algorithm was used [21], with a working point (WP) corresponding to an efficiency of 85%.

2.3.4 Missing Transverse Energy

The last SM particle that can be produced in a proton-proton collision is the neutrino. Due to its extremely small mass, the neutrino interacts only very weakly with matter, allowing it to traverse the detector almost undisturbed. The ATLAS experiment identifies these invisible particles through the computation of the $E_{\mathrm{T}}^{\mathrm{miss}}$, defined as the negative vector sum of the transverse momenta of all directly reconstructed particles (electrons, muons, jets, ecc.) and of all the tracks not associated to any physics particle, known as soft terms (ST) [22]

$$E_{\mathrm{T}}^{\mathrm{miss}} = -\left| \sum_{e} \vec{p}_{\mathrm{T}}^{\,e} + \sum_{\mu} \vec{p}_{\mathrm{T}}^{\,\mu} + \sum_{\tau} \vec{p}_{\mathrm{T}}^{\,\tau} + \sum_{\mathrm{jets}} \vec{p}_{\mathrm{T}}^{\,\mathrm{jets}} + \sum_{\mathrm{ST}} \vec{p}_{\mathrm{T}}^{\,\mathrm{ST}} \right|. \tag{2.8}$$

As previously mentioned, the total transverse momentum of the system should be zero after the collision, given that the incoming protons move along the z-axis. $E_{\mathrm{T}}^{\mathrm{miss}}$ can also be used to infer the presence of particles that are not part of the SM, such as the neutralino.

Chapter 3

Analysis Methods and Results

The analysis focuses on SUSY electroweakino pair production in final states with one or two leptons. Signal and background events were simulated using the ATLAS detector, with an integrated luminosity corresponding to the full Run 2 and part of Run 3 (2022–2023). The analysis will be finalized by subsequent studies that will also incorporate data from 2024.

This chapter outlines the analysis methods employed and reports the results obtained in the study. After describing the studied processes and the main background contributions, the concept of statistical significance is introduced, and the methods employed to discriminate between signal and background are illustrated. Finally, the obtained results are discussed, and the plots produced throughout the analysis are presented.

3.1 Overview of the Physical Processes Considered

In this section, the process under study is presented, including the possible decay channels of its products and the SM processes that constitute the main backgrounds.

3.1.1 Signal Processes

Within the scope of this analysis, the associated production of a neutralino $\tilde{\chi}_2^0$ and a chargino $\tilde{\chi}_1^\pm$ is considered. Above all the channels of decays illustrated in Equations 1.11 and 1.12, this analysis focuses on the Wh production.

The previous analyses of Run 2 focused on simplified models in which the decay channel $Wh \to \ell\nu b\bar{b}$ was assumed to have a branching ratio (BR) of 100% [23, 24]. Although the signal models used in this analysis still rely on simplified assumptions as the $\tilde{\chi}_1^\pm \to \tilde{\chi}_1^0 W$ and $\tilde{\chi}_2^0 \to \tilde{\chi}_1^0 h$ decays are both assumed with a BR=100%, this analysis takes into account the SM values of the BRs for the W and h boson mediated decays, opening up all SM decay channels for the W and h as shown in Table 3.1 [25, 26, 27]. This is the first analysis of its kind performed in Run 3.

As a consequence, the most promising channel for experimental observation is the one producing two jets (originating from the hadronic decay of the h boson), an isolated

Decay channel	BR
$W \to q\bar{q}'$	67.3%
$W \to \ell\nu_\ell$	32.7%
$Z \to q\bar{q}$	69.9%
$Z \to \nu\bar{\nu}$	20.2%
$Z \to \ell^+\ell^-$	9.9%

Decay channel	BR
$h \to b\bar{b}$	57.7%
$h \to W^+W^-$	21.5%
$h \to gg$	8.6%
$h \to \tau^+\tau^-$	6.3%
$h \to ZZ$	2.6%

Table 3.1: BRs of the W, Z and h bosons.

visible lepton (from the leptonic decay of the W boson), and significant $E_{\mathrm{T}}^{\mathrm{miss}}$ due to the presence of the undetected LSP (see Figure 3.1). This type of signature is referred to as the single charged lepton channel, which constitutes the focus of the data analysis presented in this thesis.

The dilepton topology (Figure 3.2) is also considered, in which the W boson decays into two quarks (producing two jets), while the h boson decays into a pair of visible leptons. From the BRs of the W and h bosons, it can be observed that the approximate probability of the decay $W \to \ell\nu$ occurring simultaneously with $h \to b\bar{b}$ is

$$p_{1\ell} = 0.327 \times 0.577 \approx 19\%,$$

while for the dilepton process, the probability that the decays $W \to q\bar{q}'$ and $h \to \ell^+\ell^-$ occur simultaneously is approximately

$$p_{2\ell} = 0.673 \times 0.063 \approx 4\%.$$

Although this configuration is less probable and therefore statistically less significant compared to the single lepton channel, this is the first analysis to target this channel specifically.

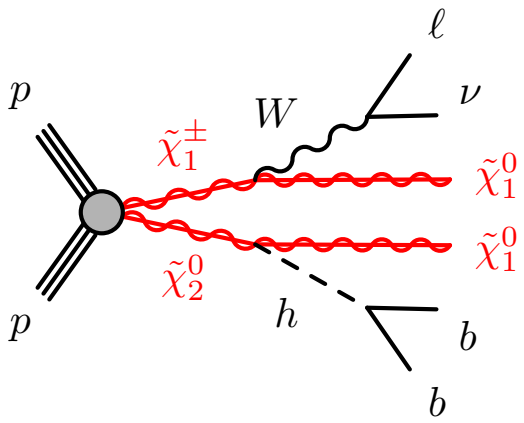

Figure 3.1: Single charged lepton channel.

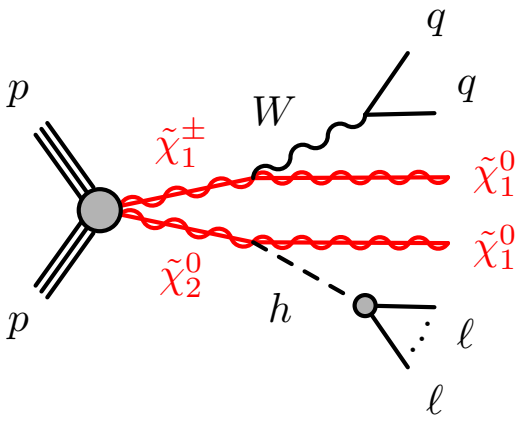

Figure 3.2: Dilepton channel.

3.1.2 Background Processes

The main background for the process are W+jets, $t\bar{t}$, Wt, diboson (WW, WZ, ZZ), Z+jets, dijet, triboson, $V+\gamma$, V+jets and the associated higgs boson production (Vh).

The background consists of SM processes, some of them can mimic SUSY events, thereby hindering their identification. These background are reconstructed with a full simulation of the ATLAS detector.

The main SM backgrounds for the single lepton channel are:

- W+jets production, when the W boson decays into a lepton and a neutrino, while the jets originate from initial state radiation. This represent the largest background at the preselection level;
- $t\bar{t}$ production, when one top quark decays as $t \to Wb$ with $W \to \ell\nu$, while the other decays as $t \to Wb$ with $W \to q\bar{q}'$;
- WW production, when one W boson decays into two light quarks, producing two jets, and the other decays into a lepton and a neutrino, yielding the observable lepton and $E_{\mathrm{T}}^{\mathrm{miss}}$ respectively;
- Wt production, the single top production associated with a W boson can produce events similar to those from WW, but with the presence of an additional b-jet;
- WZ production, when the W boson decays to a lepton and a neutrino and the Z boson to two quarks, the final state contains a lepton, $E_{\mathrm{T}}^{\mathrm{miss}}$, and two jets. In rare scenarios, if $Z \to \ell^+\ell^-$ but one lepton is not reconstructed and $W \to q\bar{q}'$, the event can appear as single lepton;
- ZZ production, when one $Z \to \ell^+\ell^-$ but one lepton is not reconstructed and the other $Z \to q\bar{q}$.

Regarding the dilepton channel, particular attention must be given to the following background processes:

- $t\bar{t}$ production: when both top quarks decay into Wb, with the W bosons subsequently decaying leptonically ($W \to \ell\nu$), the final states mimic those of the targeted signal. This process constitutes the primary background for this topology;
- WZ production: where the$W$boson decays into two quarks, and the Z boson decays into a pair of leptons; $E_{\mathrm{T}}^{\mathrm{miss}}$ may originate from secondary leptonic decays;
- ZZ production: one Z boson decays hadronically into two quarks producing two jets, while the other decays leptonically into two leptons, yielding the observable dilepton pair;
- Wt production: in cases where the top quark decays as $t \to Wb$ with both Wt bosons decaying leptonically;
- $Z+$ jets production: where the Z boson decays into a lepton-antilepton pair.

3.2 Statistical Significance

This thesis analyses the distributions of signal and background processes as a function of selected kinematic variables, which will be discussed in the following sections. These distributions are obtained through Monte Carlo (MC) simulations, in accordance with the

predictions of the SM and SUSY. The MC signal samples with $pp \to \tilde{\chi}_1^{\pm}\tilde{\chi}_2^0 \to \tilde{\chi}_1^0\tilde{\chi}_1^0 Wh$ has been generated using state of the art tools for PDF, underlying event, parton shower and hadronization.

The goal of this analysis is to evaluate the effectiveness of different methods in distinguishing signal from background. To this end, it is useful to introduce the concept of statistical significance Z_n, defined as [28]

$$Z_n = \sqrt{2\left[n\log\left(\frac{n\,(b+\sigma^2)}{b^2+n\sigma^2}\right) - \frac{b^2}{\sigma^2}\,\log\left(1+\frac{\sigma^2\,(n-b)}{b\,(b+\sigma^2)}\right)\right]}, \tag{3.1}$$

where n is the number of observed events, $n = s + b$, with s being the number of signal events and b the number of background events; and σ is the uncertainty on the background, obtained by quadratically combining systematic and statistical uncertainties. The systematic uncertainty is chosen to be 20% of b.

To understand the physical meaning expressed by the significance, one may refer to its simplified definition, namely

$$Z = \frac{s}{\sqrt{b}}, \tag{3.2}$$

where s denotes the expected number of signal events and b the expected number of background events. To avoid numerical issues, the conditions $b \geq 1$, to prevent division by zero, and $s \geq 3$, to ensure statistical relevance, are imposed.

Since background processes are subject to statistical fluctuations, often modelled using a Poisson distribution, the associated uncertainty can be approximated as $\sqrt{b}$. The statistical significance Z therefore quantifies how unlikely it is that an observed excess in the number of events is due to a mere statistical fluctuation of the background. Higher values of Z indicate a greater likelihood of detecting a genuine signal that can be distinguished from the background. In general, a region is considered significant when Z reaches values of the order of unity or higher.

In this work, the analysis focuses on the cumulative significance, defined as the sum of the significance computed bin by bin along the distribution. To refine the analysis, two integration criteria are introduced, referred to as cut left and cut right. The cut left corresponds to the cumulative sum of the significance from the left tail of the distribution up to a given bin, including all preceding bins. Conversely, the cut right refers to the cumulative sum from the right tail of the distribution down to the given bin, including all subsequent bins. The aim is therefore to maximize the statistical significance, in order to improve the separation between signal and background.

3.3 Preselection

Events are first required to satisfy a logical OR between the presence of a single lepton and $E_{\mathrm{T}}^{\mathrm{miss}} > 200$ GeV.

They are then selected through the event cleaning process, which discards events not associated with a primary interaction vertex, an essential feature for identifying a

genuine collision, events with noise bursts or data integrity errors in the LAr and Tile calorimeters, events with SCT errors, and events containing poorly reconstructed muons and jets.

Finally, candidate events are selected by applying a preselection, which consists on requirements on the number of photons, n_γ, with transverse momentum $p_\mathrm{T} > 7\,\mathrm{GeV}$, on the number of leptons (electrons or muons), n_leptons, with $p_\mathrm{T} > 7\,\mathrm{GeV}$, on the number of jets, n_jets with $p_\mathrm{T} > 30\,\mathrm{GeV}$ and on the missing transverse energy $E_\mathrm{T}^\mathrm{miss}$. The requirements applied at the preselection level are reported in Table 3.2.

Variable	**Selection**
$n_\gamma^{p_\mathrm{T}>7\,\mathrm{GeV}}$	$= 0$
$n_\mathrm{leptons}^{p_\mathrm{T}>7\,\mathrm{GeV}}$	$\in [1, 2]$
$n_\mathrm{jets}^{p_\mathrm{T}>30\,\mathrm{GeV}}$	≥ 1
$E_\mathrm{T}^\mathrm{miss}$	> 200 GeV

Table 3.2: Preselection requirements.

The distributions of the event yields for the various processes were studied Within the preselection region as functions of the following kinematic variables:

- $p_\mathrm{T}^{\ell_1}$, which is the transverse momentum of the leading lepton. This variable is useful for distinguishing signal from background, as signal events typically occur at higher energies, producing leptons with higher momentum.
- $E_\mathrm{T}^\mathrm{miss}$. Signal processes which involve neutralinos generally exhibit higher $E_\mathrm{T}^\mathrm{miss}$ values than those measured in background processes.
- n_leptons, the number of leptons, which can be either one or two. The signal process is expected to be more abundant for the one lepton channel than for the dilepton one, as previously explained.
- n_jets, the number of jets, which are selected to be greater or equal than one from the preselection requirements.
- $n_\mathrm{b\text{-}jets}$, the number of b-jets, which can be zero or more given that this variable is not considered in the preselection. It is possible to notice that there is a peak in the significance at $n_\mathrm{b\text{-}jets} = 2$, as expected from the final state of the single charged lepton channel shown in Figure 3.1.
- $n_\mathrm{boosted\ jet}$, the number of boosted jets. It is visible that signal processes with at least one boosted jet are more abundant than those involving only resolved jets. Indeed, the significance is peaked for $n_\mathrm{boosted\ jet} = 1$.

To estimate the behaviour of the kinematic variables in the signal processes, it is necessary to assign specific values to the free parameters of the neutralino and chargino masses. For this reason, the set of considered mass hypotheses is listed in Table 3.3. Above all, the benchmarks considered are $m(\tilde{\chi}_1^\pm/\tilde{\chi}_2^0,\ \tilde{\chi}_1^0) = (200, 50)$ GeV, $(400, 50)$ GeV, $(600, 50)$ GeV, $(600, 450)$ GeV and $(800, 0)$ GeV.

$\Delta m(\tilde{\chi}_1^{\pm}/\tilde{\chi}_2^0, \tilde{\chi}_1^0)$ (GeV)	$m(\tilde{\chi}_1^{\pm}/\tilde{\chi}_2^0, \tilde{\chi}_1^0)$ (GeV)
150	$(200, 50)$ $(350, 200)$ $(600, 450)$
200	$(400, 200)$ $(450, 250)$ $(500, 300)$ $(600, 400)$
250	$(450, 200)$ $(500, 250)$ $(550, 300)$ $(600, 400)$
300	$(600, 300)$
350	$(400, 50)$ $(650, 300)$ $(800, 450)$
400	$(700, 300)$ $(800, 400)$
450	$(750, 300)$
500	$(800, 300)$
550	$(600, 50)$
600	$(800, 200)$ $(900, 300)$
700	$(800, 100)$ $(900, 200)$ $(1000, 100)$
750	$(800, 50)$
800	$(800, 0)$ $(900, 100)$ $(1000, 200)$
850	$(900, 50)$
900	$(900, 0)$ $(1000, 100)$
950	$(1000, 50)$
1000	$(1000, 0)$ $(1100, 100)$
1050	$(1100, 50)$
1100	$(1100, 0)$ $(1200, 100)$
1150	$(1200, 50)$
1200	$(1200, 0)$

Table 3.3: Sets of mass values for charginos/neutralinos and LSP considered in the analysis.

The variables at the preselection level are shown in Figure 3.3. In each plot, the upper panel displays the distribution of the signal and the main background processes, while the lower panel reports the behaviour of the cumulative significance, calculated by applying a cut right. It can be observed that, in this region, the significance values are two orders of magnitude below one.

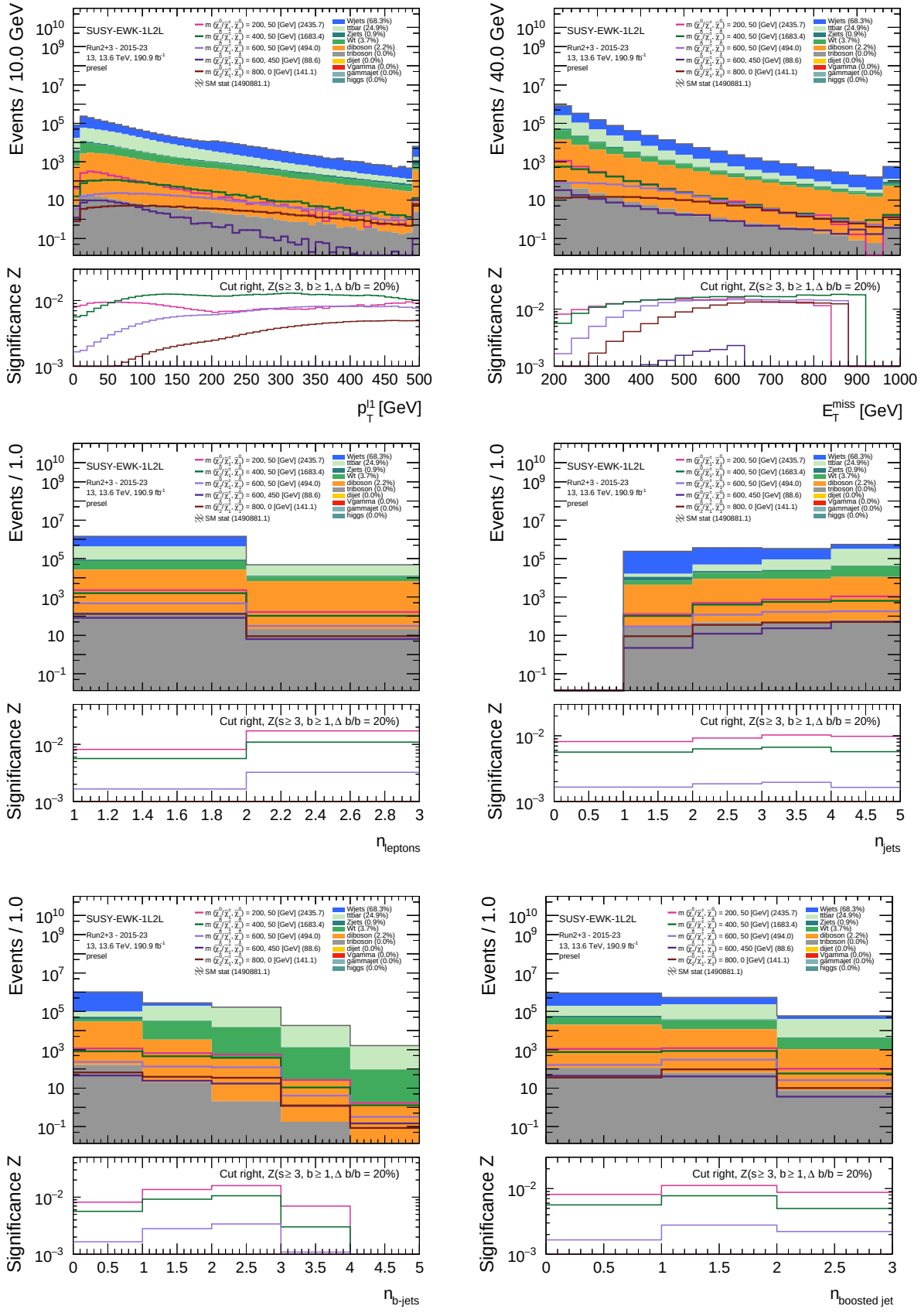

Figure 3.3: Distributions of signal and background processes for the benchmark mass hypotheses with respect to the variables $p_{\mathrm{T}}^{\ell_1}$, $E_{\mathrm{T}}^{\mathrm{miss}}$, n_{leptons}, n_{jets}, $n_{\mathrm{b\text{-}jets}}$ and $n_{\mathrm{boosted\ jets}}$. The bottom panel shows the behaviour of the significance calculated by applying a cut right.

3.4 Single Lepton Channel

Since it is statistically more frequent, the analysis in this thesis focuses primarily on the single lepton channel.

3.4.1 Definition of Signal Regions

A signal region (SR) is a subset of the phase space (for example defined by invariant mass, missing transverse energy, or other observables), optimized to maximize signal yield while suppressing background. To improve the statistical significance of the single lepton channel, the C&C analysis method was chosen. In this method, SRs are defined by applying selection cuts on discriminating kinematic variables.

The choice is based on the kinematics of the processes under study, which depend on the masses of the produced states.

The value of $\Delta m = m_{\tilde{\chi}_1^\pm/\tilde{\chi}_2^0} - m_{\tilde{\chi}_1^0}$ has a significant impact on the kinematic properties of the final-state particles. As Δm increases, the decay products of the signal tend to be more energetic, making them more easily distinguishable from SM backgrounds. However, this improvement in signal visibility comes at the cost of a lower production cross section, since heavier parent SUSY particles are produced less frequently. To account for this trade-off between signal detectability and production rate, several benchmark mass points have been considered, as listed in Table 3.3, exploring different combinations of parent and daughter masses, which are still unknown from an experimental point of view.

Events with low, medium, and high Δm can be distinguished by studying the transverse mass m_{T}. This kinematic variable is particularly suitable for processes where a parent particle decays into two daughter particles, one visible and one invisible, such as in the case of $W \to \ell\nu$. The transverse mass allows reconstructing the mass of the parent particle. In natural units, m_{T} is defined as [23]

$$m_{\mathrm{T}}^2 = 2\, p_{\mathrm{T}}^{\ell}\, E_{\mathrm{T}}^{\mathrm{miss}}\, (1 - \cos\Delta\phi)\,,$$

where p_{T}^{ℓ} is the transverse momentum of the visible particle (e.g., the lepton), $E_{\mathrm{T}}^{\mathrm{miss}}$ represents the energy of the invisible particle (in our example, the neutrino), and $\Delta\phi$ is the angle between the two vectors in the plane transverse to the collision.

In the calculation of m_{T}, $E_{\mathrm{T}}^{\mathrm{miss}}$ is considered to be due exclusively to SM particles; therefore, in SUSY process studies, m_{T} is more accurately regarded as a good estimate of Δm, since it also takes into account the mass of $\tilde{\chi}_1^0$, rather than the mass of the parent particle.

Considering the decay $h \to b\bar{b}$, in which two visible objects are produced, one can exploit the variable called the contransverse mass, defined as [23]

$$m_{\mathrm{CT}}^2 = 2 p_{\mathrm{T}}^{b_1} p_{\mathrm{T}}^{b_2} (1 + \cos\Delta\phi_{bb}), \tag{3.3}$$

where $p_{\mathrm{T}}^{b_{1/2}}$ denotes the transverse momentum of the two b-jets, and $\Delta\phi_{bb}$ is the azimuthal angle between them. The variable m_{CT} allows for the suppression of one of the main

backgrounds in the preselection region, namely the $t\bar{t}$ process, for which this quantity is kinematically bounded to values below approximately 180 GeV.

Several regions were explored by varying the selections on these variables and the SR selection is chosen as the combination of cuts that maximizes the significance. The defined SRs are listed in Table 3.4 [23]. In each of the six regions, the conditions of trigger matching and preselection are also applied. The acronyms SRLM, SRMM, and SRHM denote SRs characterized by low, medium, and high Δm, respectively. Accordingly, based on the considerations outlined above, one expects higher significance in the LM regions for mass hypotheses with low mass splitting, while the HM regions are predicted to exhibit greater significance for mass hypotheses with high Δm.

Finally, a distinction is made between boosted and resolved regions, regarding processes which are connected respectively to the detection of boosted jets and resolved jets. The presence or absence of boosted jets is a key indicator of the process's energy scale. Both cases are considered in the analysis.

SR	$n_{b\text{-jets}}$	E_{T}^{miss} (GeV)	m_{T} (GeV)	m_{CT} (GeV)	$n_{\text{boosted jets}}$
SRLM-1L-resolved	2	> 240	$\in [100, 160)$	> 180	0
SRMM-1L-resolved	2	> 240	$\in [160, 240)$	> 180	0
SRHM-1L-resolved	2	> 240	≥ 240	> 180	0
SRLM-1L-boosted	2	> 240	$\in [100, 160)$	> 180	≥ 1
SRMM-1L-boosted	2	> 240	$\in [160, 240)$	> 180	≥ 1
SRHM-1L-boosted	2	> 240	≥ 240	> 180	≥ 1

Table 3.4: Definition of the SRs based on considerations of the kinematic nature of the process.

Choice of Cuts

In this subsection, the choices of the applied cuts are justified by analysing the variable distributions and the behaviour of the statistical significance Z.

Figure 3.4 shows the signal and background distributions within the previously defined SRs, with the condition on the variable under study removed in each case. For clarity, each SR from which a distribution is obtained is labelled with its original SR name, appended with the suffix "-var," where "var" indicates the variable whose cut condition has been removed.

It is observed that in (a), there is signal statistics only when $n_{b\text{jets}} = 2$, due to the cut on m_{CT}, and from (f), only when $n_{\text{boosted jets}} \geq 1$. From (b), a peak in the significance is seen for the variable $E_{\mathrm{T}}^{\mathrm{miss}}$ around the value chosen for the cut. The same behaviour is observed for the medium mass splitting region in (c) and (d), where the transverse mass m_{T} shows a clear maximum in Z around the selected threshold. Finally, from (e) it can be observed that applying a cut of $m_{\mathrm{CT}} > 180$ GeV removes most of the $t\bar{t}$ background. These behaviours confirm that the selected combination of cuts described in Table 3.4 represents an optimal choice for maximizing the statistical significance.

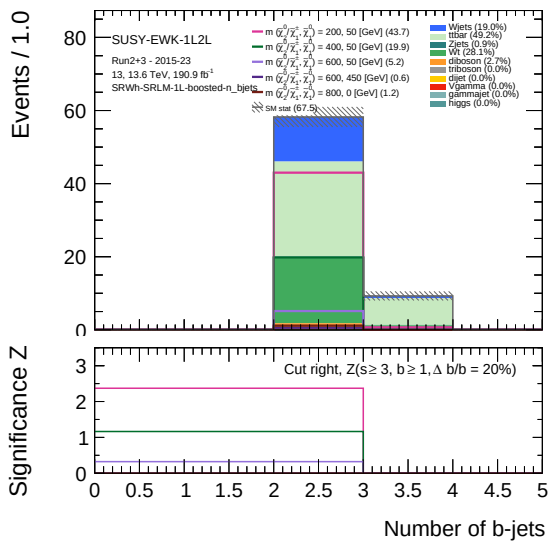

(a) Distribution of $n_{b\text{-jets}}$ for the benchmark mass hypotheses.

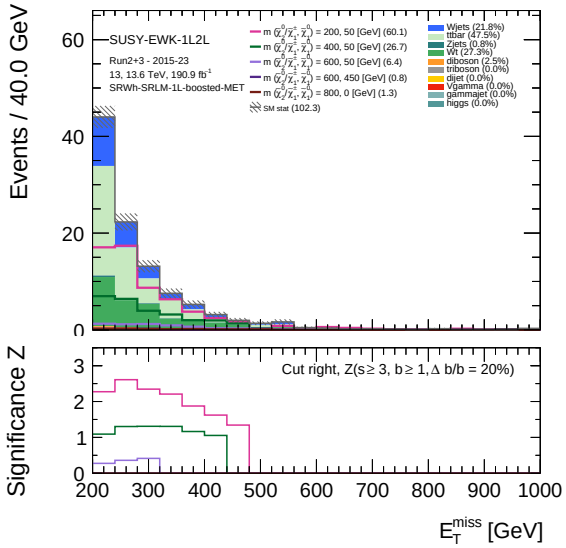

(b) Distribution of $E_{\mathrm{T}}^{\mathrm{miss}}$ for the benchmark mass hypotheses.

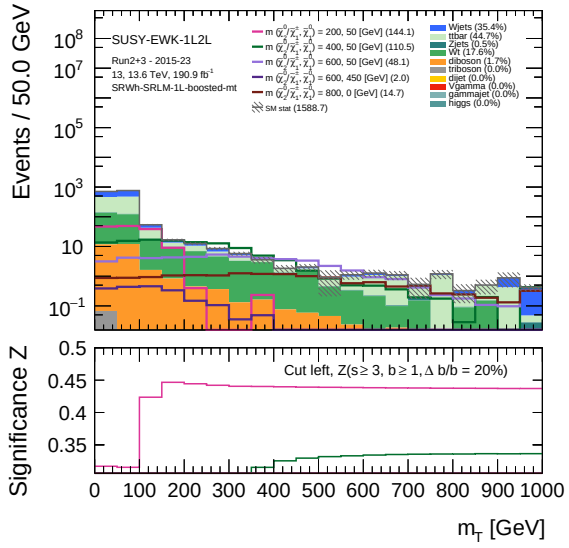

(c) Distribution of m_{T} for the benchmark mass hypotheses. In the bottom panel the trend of Z is shown with a cut left.

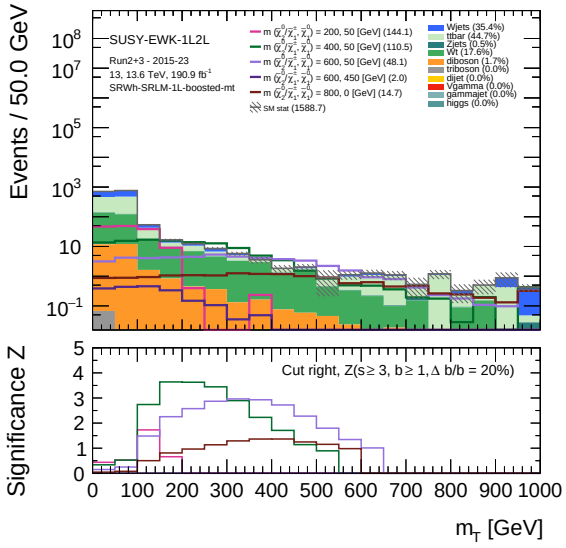

(d) Distribution of m_{T} for the benchmark mass hypotheses. In the bottom panel the trend of Z is shown with a cut right.

Figure 3.4

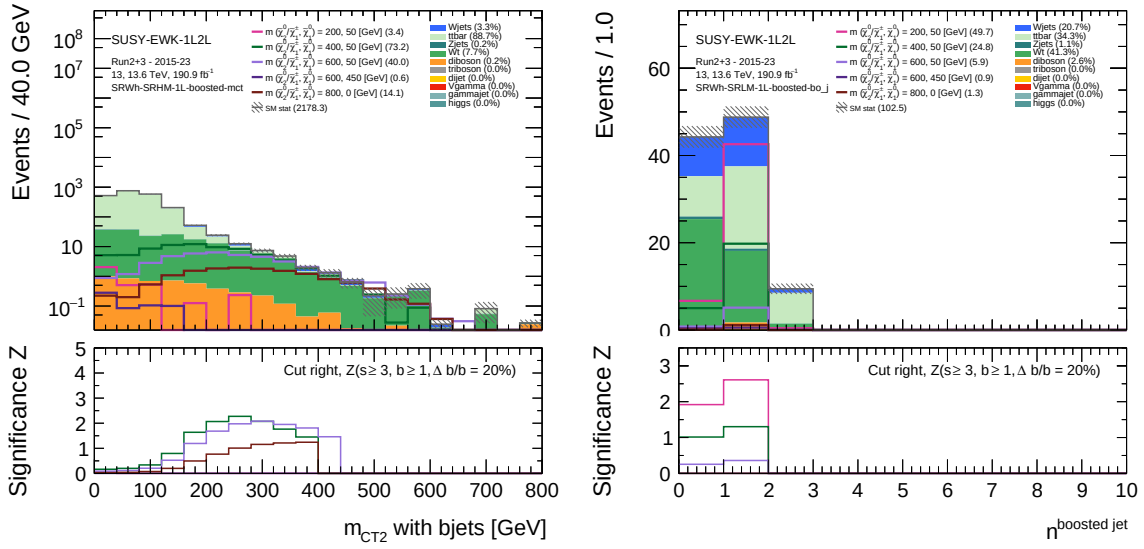

(e) Distribution of m_{CT} for the benchmark mass hypotheses.

(f) Distribution of $n_{\text{boosted jets}}$ for the benchmark mass hypotheses.

Figure 3.4: (Continued)

Distributions for SRs

The background and signal distributions were derived for the following variables:

- $E_{\mathrm{T}}^{\mathrm{miss}}$, which is expected to be higher in signal processes than in those considered for the background due to the presence of undetected SUSY particles.
- $\Delta\phi(\ell_1, E_{\mathrm{T}}^{\mathrm{miss}})$, the angle in the transverse plane between the direction of the lepton and that of the $E_{\mathrm{T}}^{\mathrm{miss}}$. In background processes, the $E_{\mathrm{T}}^{\mathrm{miss}}$ primarily originates from the neutrino produced alongside the lepton. In signal events the $E_{\mathrm{T}}^{\mathrm{miss}}$ also includes contributions from the two LSPs, resulting in a different distribution of this variable compared to the background.
- m_{jj}, the invariant mass of the two jets. In the case of the signal, the two jets originate from the decay of the Higgs boson; therefore, one expects a peak in the distribution near the Higgs mass, approximately $m_h = 125$ GeV. For this reason, this variable serves as an excellent discriminator to distinguish signal from background.

The resulting distributions are shown in Figures 3.5, 3.6, and 3.7. The first figure shows the distribution with respect to the variable $E_{\mathrm{T}}^{\mathrm{miss}}$ in the six SRs, where the condition $E_{\mathrm{T}}^{\mathrm{miss}} > 240$ GeV was intentionally removed to highlight that the statistical significance peaks around this value. The remaining figures display the signal and background distributions with respect to the variables $\Delta\phi(\ell_1, E_{\mathrm{T}}^{\mathrm{miss}})$ and m_{jj} in the top panel, while the bottom panel shows the behaviour of the statistical significance Z both with cuts left and right.

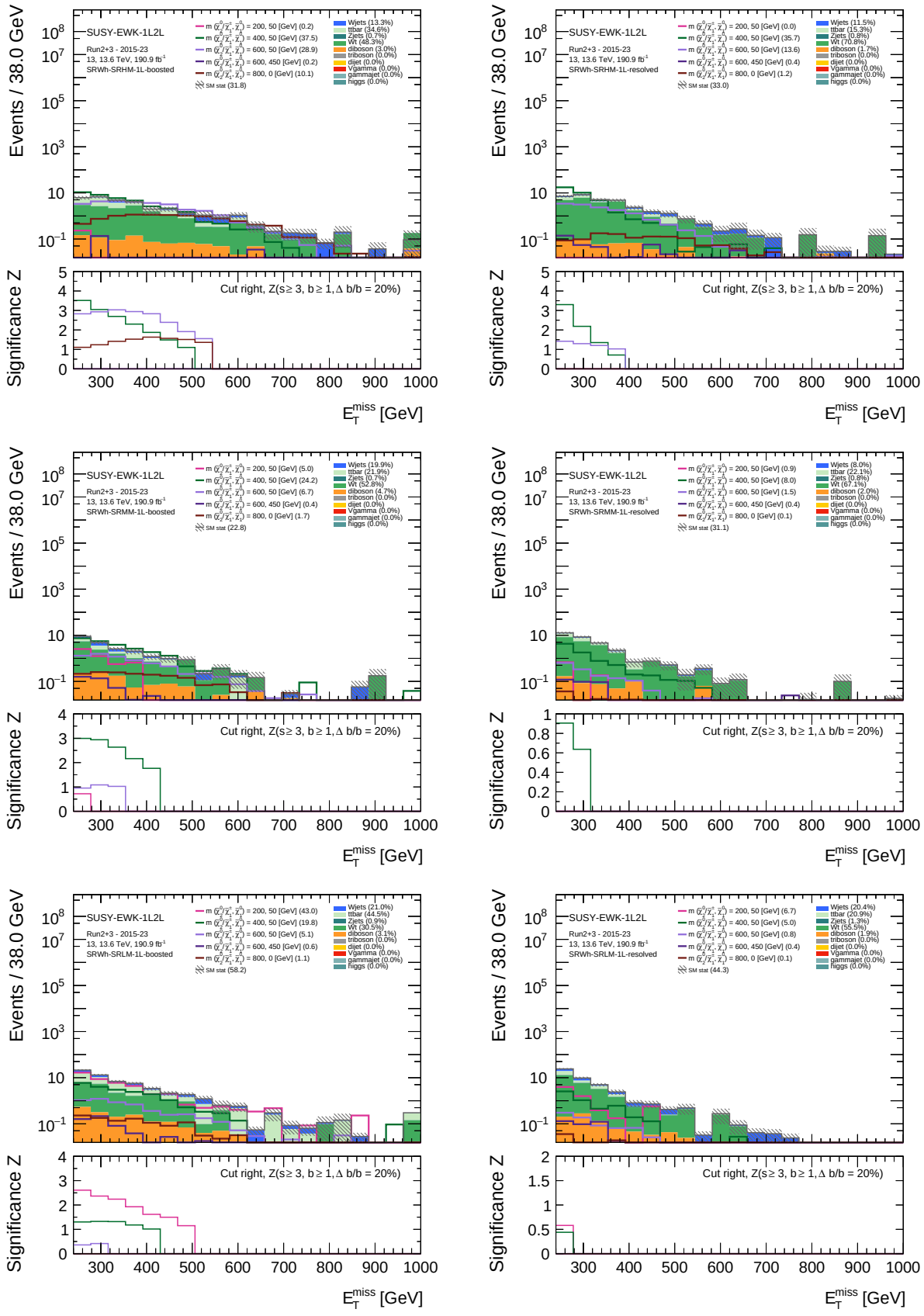

Figure 3.5: The top panels display the distributions of signals of benchmark mass hypotheses for the variable $E_{\mathrm{T}}^{\mathrm{miss}}$ within the six considered SRs. The bottom panels show the behaviour of the significance calculated with a cut right.

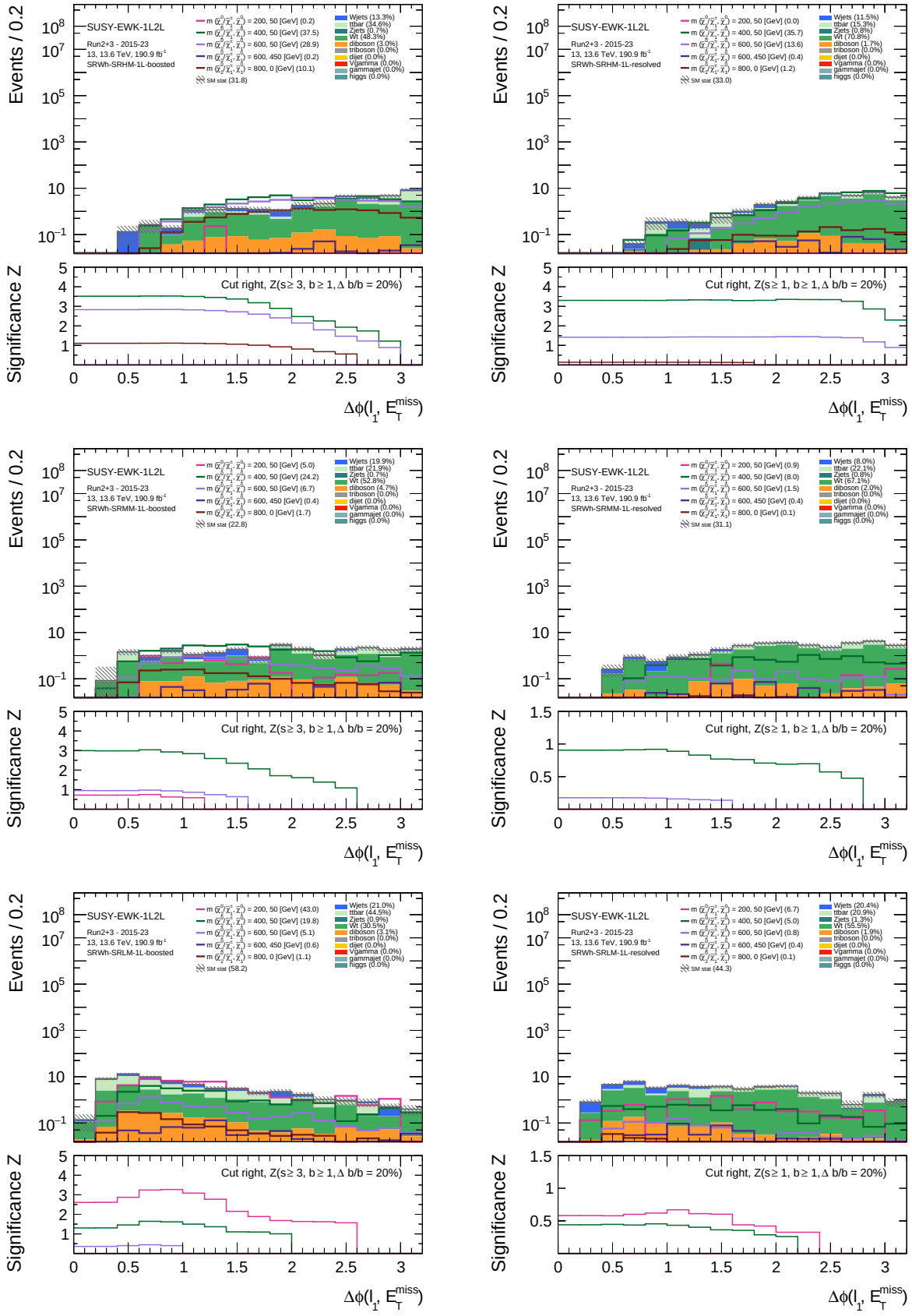

Figure 3.6: The top panels display the distributions of benchmark mass hypotheses for the variable $\Delta\phi(\ell_1, E_{\mathrm{T}}^{\mathrm{miss}})$ within the six considered SRs. The bottom panels show the behaviour of the significance calculated with a right cut applied.

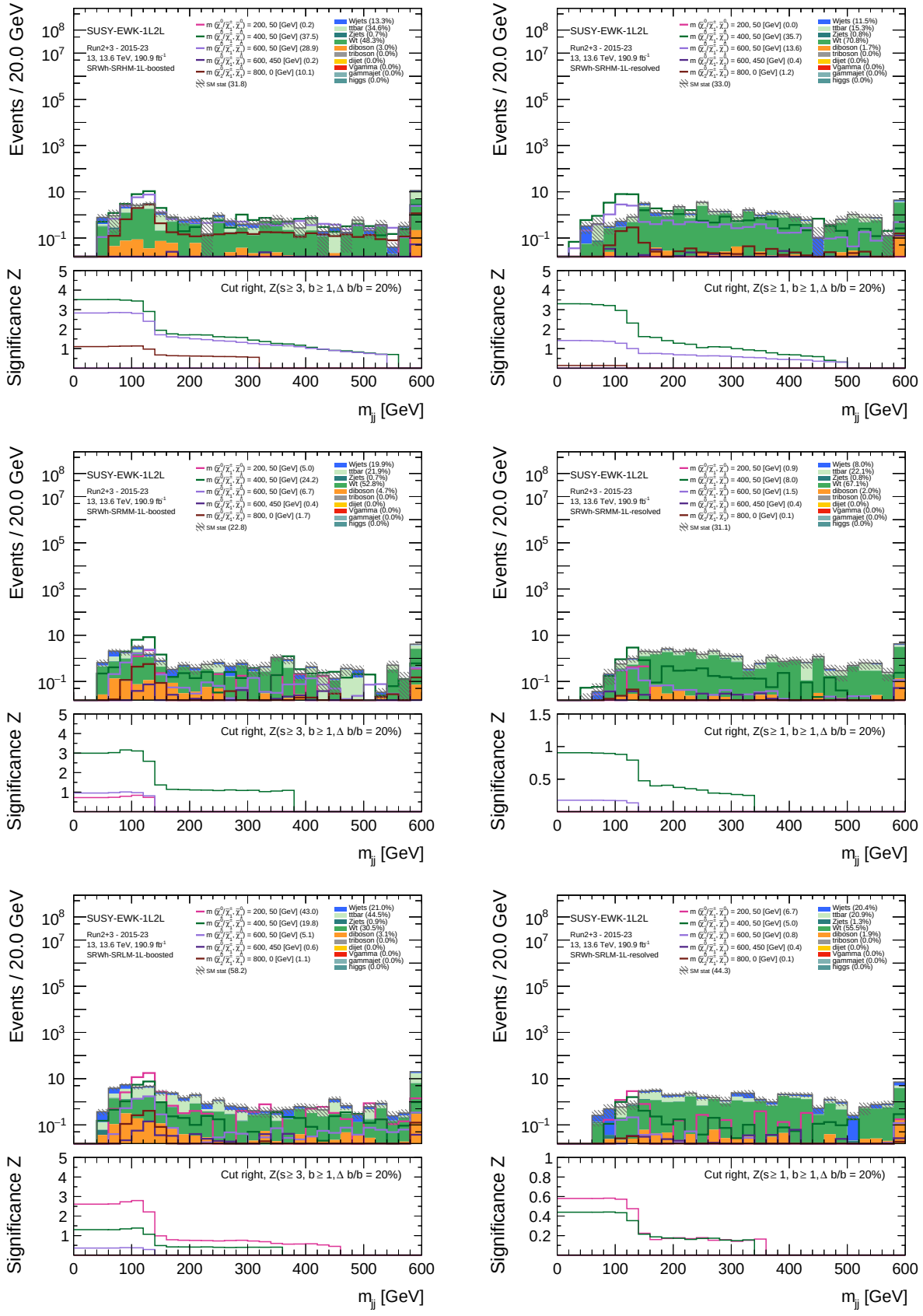

Figure 3.7: The top panels display the distributions of benchmark mass hypotheses for the variable m_{jj} within the six considered SRs. The bottom panels show the behaviour of the significance calculated with a right cut applied.

3.5 Dilepton Channel Analysis

In this section, the dilepton channel illustrated in Figure 3.2 is analysed. As previously explained, this channel is rarer compared to the single lepton channel, and consequently, lower significance values are expected.

The study was performed within the region defined as 2ℓ, where events are required to pass the trigger matching and the criterion of containing two reconstructed leptons. As we will see from the plots in the dilepton channel, the significance values are very low, reflecting the rarity of having two reconstructed leptons compared to the case of having one reconstructed lepton, as expected from the BR comparison we discussed. A SR in 2ℓ can be defined by introducing a series of cuts on variables that we defined for the single-lepton channel and other specific ones for the dilepton channel. In particular, the study of the number of boosted jets, $n_{\text{boosted jets}}$, whose distribution is shown in Figure 3.8, suggests defining a SR, named 2L-boosted, obtained by adding the following condition to the selection of the 2L region

$$n_{\text{boosted jets}} \geq 1. \tag{3.4}$$

This choice is motivated by the fact that, in high-energy events, the W boson can be sufficiently boosted to produce a single jet containing both quarks.

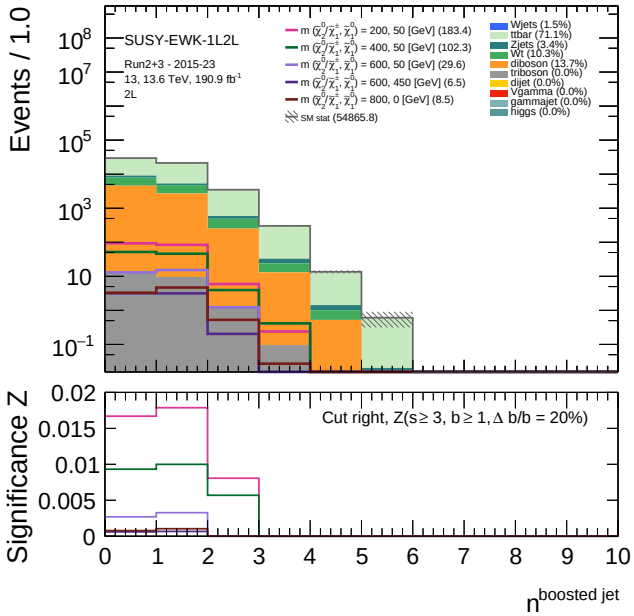

Figure 3.8: Distributions of the signal within the 2ℓ region for the variable $n_{\text{boosted jet}}$.

Subsequently, the distribution of the variable $m_{\text{boosted jet 1}}$, representing the mass of the most energetic boosted jet, is analysed. If the W boson is sufficiently energetic and decays into a qq' pair, the two jets can be reconstructed as a single boosted jet, whose mass is expected to peak around m_W. This variable is useful for discriminating signal from the $t\bar{t}$ background, where the two quarks do not originate from the same W boson and therefore do not exhibit a peak at m_W. Figure 3.9 shows the distribution of this variable within the 2L-boosted region, applying both left and right cumulative significance cuts.

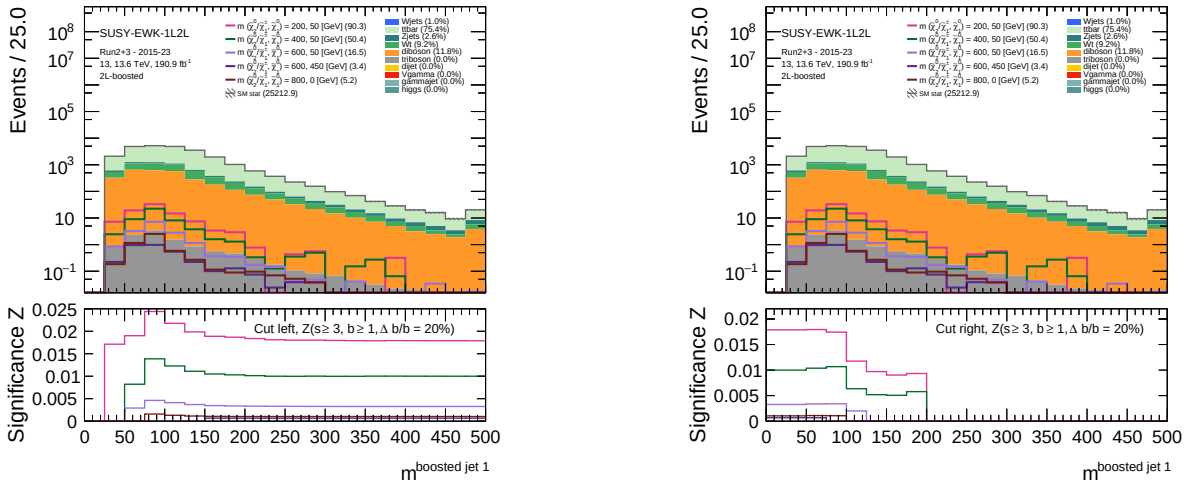

Figure 3.9: Distributions of the signal within the 2L-boosted region for the variable $m_{\text{boosted jet 1}}$.

This study reveals an improvement in significance when imposing the following condition

$$50 \text{ GeV} \leq m_{\text{boosted jet 1}} \leq 100 \text{ GeV}, \tag{3.5}$$

which defines the new SR 2L-boosted-mcut. This result is consistent with the physical expectation that the boosted jet should have a mass compatible with that of the W boson.

A further variable of interest is $m_{\ell_1\ell_2}$, the invariant mass of the system composed of the two leptons. Although in this channel the two leptons originate from the decay of the h boson, the process of h decaying into muons or electrons is highly suppressed due to their low mass. More generally, the two leptons arise from subsequent decays involving several intermediate states. Therefore, no peak is expected in the invariant mass distribution. The distribution of this variable in the 2L-boosted-mcut region (Figure 3.10) shows that it is not beneficial to apply an additional cut on this variable.

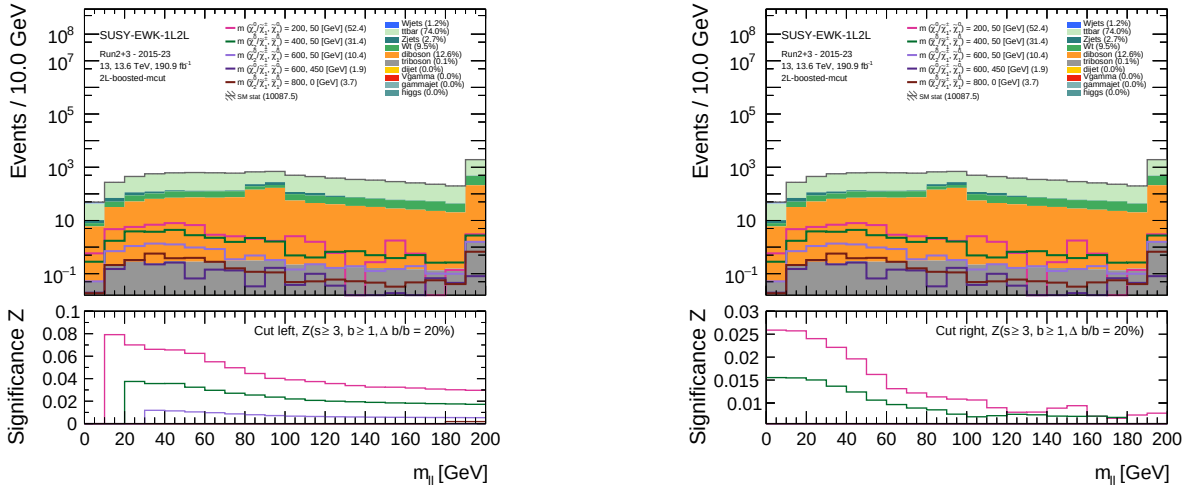

Figure 3.10: Distributions of the signal within the 2L-boosted-mcut region for the variable $m_{\ell_1\ell_2}$.

The analysis of the left-cut significance trend indicates that, for smaller mass splitting the position of the significance peak shifts to lower values, as expected.

The analysis then continues with the variable $p_{\mathrm{T}}^{\ell_1\ell_2}$, which is the vector sum of the transverse momentum of the two produced leptons, defined as

$$p_{\mathrm{T}}^{\ell\ell} = \left|\vec{p}_{\mathrm{T}}^{\,\ell_1} + \vec{p}_{\mathrm{T}}^{\,\ell_2}\right|. \tag{3.6}$$

The study of this variable is particularly useful for discriminating signal from background. Indeed, in processes like the one considered here, the two leptons originate from the decay of the h, and therefore their transverse momentum directions tend to be correlated with that of the mother particle. Conversely, in background processes, the two leptons may come from distinct mother particles, often resulting in widely separated transverse momenta. This leads to generally higher values of $p_{\mathrm{T}}^{\ell_1\ell_2}$ for the signal compared to the background.

The results of the analysis, shown in Figure 3.11, suggest introducing an additional cut, thereby defining the region 2L-boosted-pcut with

$$80 \text{ GeV} \leq p_{\mathrm{T}}^{\ell_1\ell_2} \leq 180 \text{ GeV}. \tag{3.7}$$

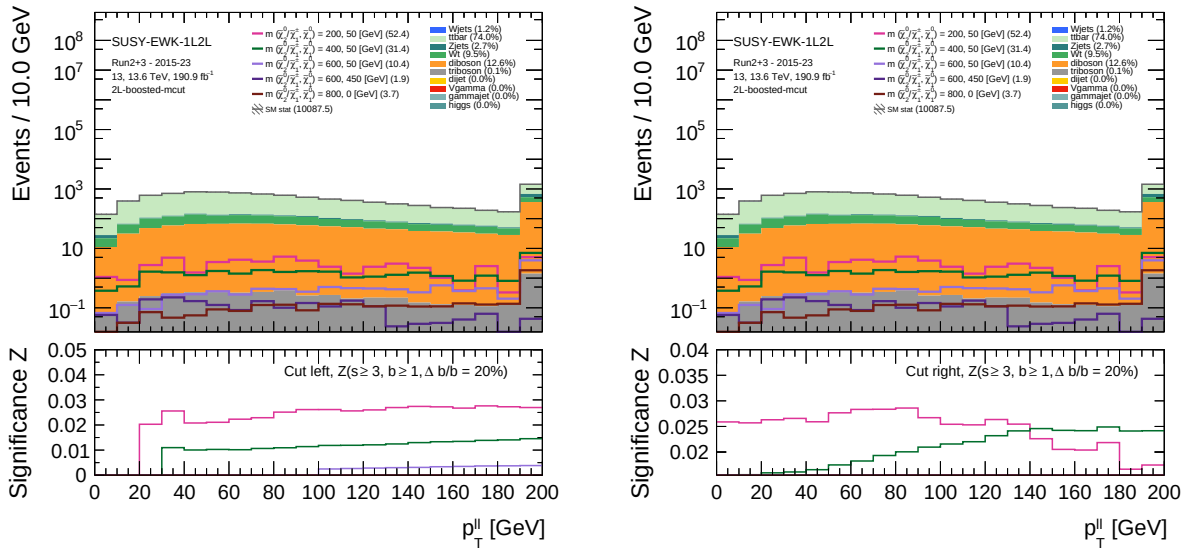

Figure 3.11: Distributions of the signal within the 2L-boosted-mcut region for the variable $p_{\mathrm{T}}^{\ell_1\ell_2}$.

Next, the variable $\Delta\phi(\ell_1, \ell_2)$ is examined in Figure 3.12. It represents the azimuthal angle between the directions of the two leptons in the transverse plane, measured with respect to the beam axis. For the signal, this variable tends to exhibit a distribution concentrated at relatively small values, reflecting a stronger angular correlation, whereas in background processes the distribution appears more uniform and less distinctive. From the plots an improvement in significance is observed for small azimuthal angle values. Therefore, the region 2L-boosted-phicut is defined by imposing

$$\Delta\phi(\ell_1, \ell_2) \leq 1.0 \text{ rad}. \tag{3.8}$$

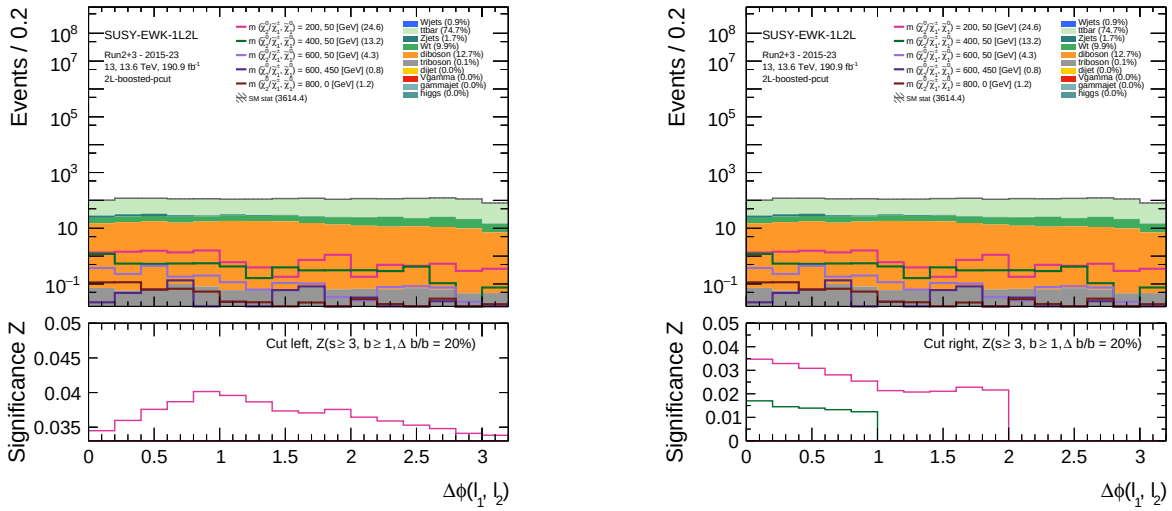

Figure 3.12: Distributions of the signal within the 2L-boosted-pcut region for the variable $\Delta\phi_{\ell_1\ell_2}$.

Finally, to further refine the signal region, the variable $\Delta R_{\ell_1\ell_2}$, which represents the angular distance between the two leptons in the pseudorapidity–azimuthal plane, is examined. Similarly as for $\Delta\phi_{\ell_1\ell_2}$, for signal processes the distribution is expected to be concentrated at low values of ΔR, indicative of more closely spaced leptons, while the background tends to show a broader distribution with generally higher values. The analysis of this variable, (Figure 3.13) shows that it is useful to define a new SR named 2L-boosted adding the cut

$$\Delta R_{\ell_1\ell_2} \leq 1.0 \text{ rad.} \tag{3.9}$$

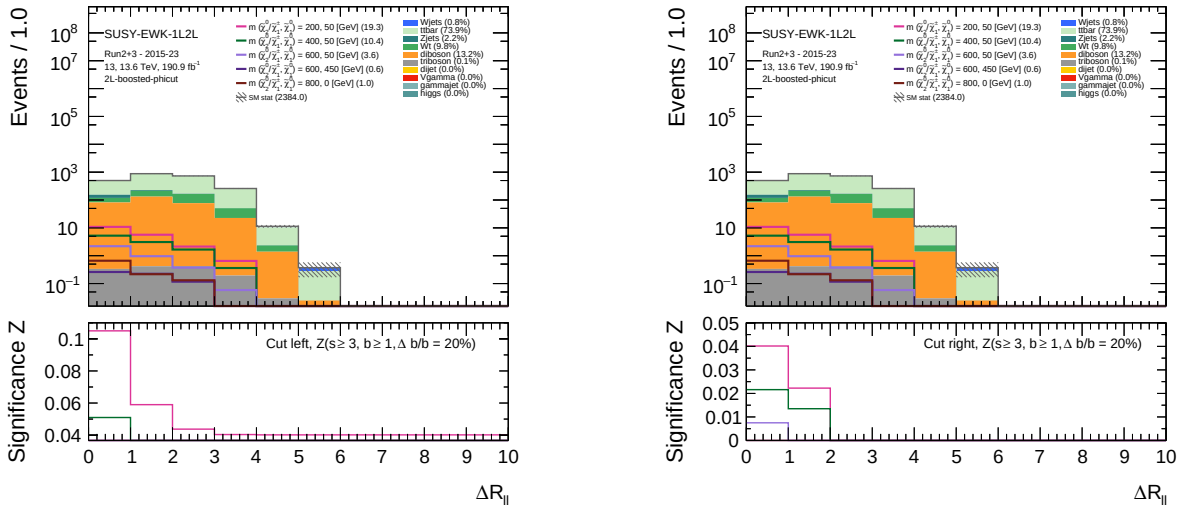

Figure 3.13: Distributions of the signal within the 2L-boosted-pcut region for the variable $\Delta R_{\ell_1\ell_2}$.

The values of Z for the signal assuming a mass hierarchy of $(200, 50)$ GeV are compared between the regions 2L and 2L-boosted, from which an improvement in statistical significance is observed:

$$Z_{\text{2L}} = 0.017 \qquad Z_{\text{2L-boosted}} = 0.105. \tag{3.10}$$

3.6 Machine Learning

The Cuts & Count method, although capable of improving the statistical significance value Z, presents several limitations, especially when analysing large or complex datasets. In such cases, it is often more effective to employ Machine Learning (ML) techniques, which can efficiently process larger volumes of data and automatically extract meaningful patterns.

ML is a branch of Artificial Intelligence that enables an algorithm to learn relationships and structures from input data, with the goal of making predictions or performing classifications. In the context of this thesis, the model is used to perform a classification task by distinguish signal from background events.

3.6.1 Deep Neural Network

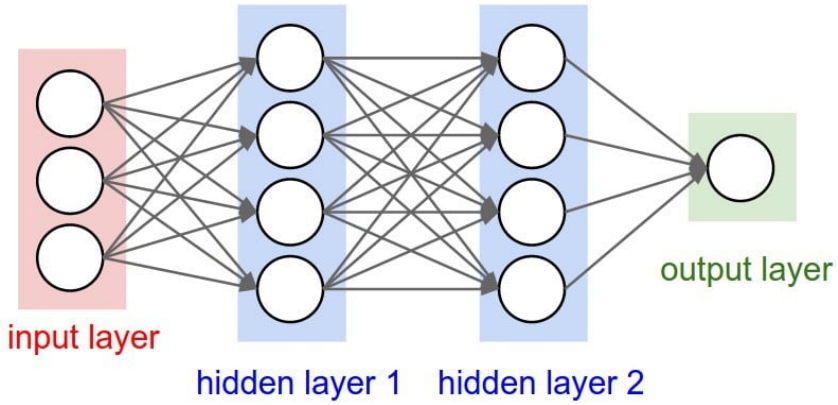

Figure 3.14: Generic structure of a DNN.

Among the most widely used ML techniques in data analysis is the DNN, a type of artificial neural network inspired by the functioning of biological neural networks. A DNN consists of a sequence of layers of artificial neurons, as shown in Figure 3.14 organized as follows:

- **input layer**, which receives the explanatory variables of the event;
- **hidden layers**, where the input data are processed through linear combinations and non-linear transformations;
- **output layer**, which returns the probability that an event belongs to the signal or background class.

In a fully connected DNN, each neuron in a layer is connected to all neurons in the previous and following layers. Each neuron receives an input vector $X = (x_1, x_2, \ldots, x_n)$, which is processed using a vector of weights $W = (w_1, w_2, \ldots, w_n)$ and a bias term b. The result is then passed through an activation function Φ, which is defined for each layer. The operation performed by a neuron can be expressed by the following equation

$$h_W(X) = \Phi(X^T W + b). \tag{3.11}$$

The input vector to the DNN consists of a set of carefully selected features that characterize each event. These features include both low-level observables, such as the transverse momentum or pseudorapidity of leptons and jets, and high-level variables, such as invariant masses, angular separations, or event-shape quantities. The choice of input features is crucial to maximize the discriminating power of the network and is based on physical intuition and preliminary studies of variable importance.

In this analysis the DNN was implemented as a sequential model [29] using the `Keras` [30] library within `TensorFlow` [31], as it is shown in Figure 3.15. The input layer receives the features listed in Table 3.5, indicated with their code name and their symbol. The

Input feature	**Symbol**
`met_GEV_NOSYS`	$E_{\mathrm{T}}^{\mathrm{miss}}$
`mT_GEV_NOSYS`	m_{T}
`lep1_Pt_GEV_NOSYS`	$p_{\mathrm{T}}^{\ell_1}$
`jet1_Pt_GEV_NOSYS`	$p_{\mathrm{T}}^{j_1}$
`jet2_Pt_GEV_NOSYS`	$p_{\mathrm{T}}^{j_2}$
`jet1MET_deltaPhi_NOSYS`	$\Delta\phi(j_1, E_{\mathrm{T}}^{\mathrm{miss}})$
`lep1MET_deltaPhi_NOSYS`	$\Delta\phi(\ell_1, E_{\mathrm{T}}^{\mathrm{miss}})$
`bjet1bjet2_M_GEV_NOSYS`	$m_{b_1 b_2}$
`bjet1bjet2_deltaR_NOSYS`	$\Delta R(b_1, b_2)$

Table 3.5: List of input features used as inputs to the DNN, along with their corresponding physical symbols.

network includes three hidden layers, each containing 100 neurons. The chosen activation function is the ReLU (Rectified Linear Unit), defined as

$$\mathrm{ReLU}(z) = \max(0, z) \tag{3.12}$$

To improve the performance of the network and reduce the risk of over-fitting, two techniques were employed:

- The adaptive moment estimation (`Adam`) optimizer [32], that can be thought as an improved gradient descent method: it keeps track of an exponentially decaying average of past gradients and combines them according to a learning rate fixed by the user.
- The `Dropout` technique, which randomly deactivates a fraction p of the neurons at each training step. This variation in information flow helps make the model more robust and generalizable. In this analysis, a dropout rate of $p = 0.2$ was used, which is a commonly adopted value in the literature.

The training and test sets are split such that they both contain half of the total MC samples, according to the `EventNumber` being odd or even. In this way, each half of the dataset is inferred from a different classifier trained on the other half and the entire signal and background samples get inferred independently.

Finally, the output layer consists of a single neuron, whose value ranges between 0 and 1. This number represents the probability that the event under analysis is classified

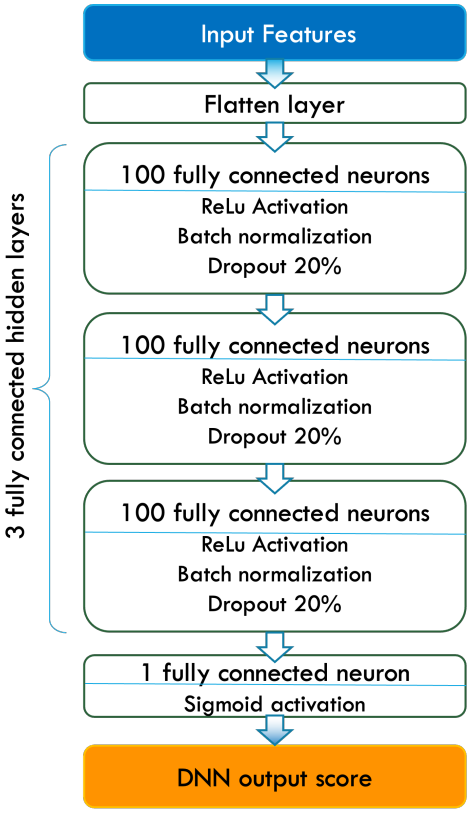

Figure 3.15: Internal structure of the DNN used in the data analysis.

as signal (values close to 1) or background (values close to 0). This output is referred to as the DNN score and is used in subsequent stages of the analysis to perform event selection.

In this analysis, a multiclass DNN was developed and trained to discriminate signal events from background processes. The network features six output classes: DNN_WH_200_50, DNN_WH_400_50, DNN_WH_600_50, DNN_WH_600_450, DNN_WH_800_0, and DNN_WH_background. Each of the first five corresponds to one of the predefined benchmark mass hypotheses, while the background class collects all non-signal events. Since the network is a multiclass DNN, the sum of the output scores across all classes is constrained to be one.

The initial evaluation of the DNN performance was carried out within a preselection region, referred to as 1Lbb. In addition to the requirements of the preselection region, this region selects events containing exactly one reconstructed lepton and two b-tagged jets. The corresponding output score distributions are presented in Figure 3.16.

In an ideal scenario, a multiclass DNN would be expected to return an output score of 1 for the correct signal class (e.g., a signal with a mass splitting of 800 GeV in the class DNN_WH_800_0) and 0 for all other classes, including the background. In practice, however, this behaviour is not observed. Owing to the multiclass architecture, the output scores are normalized such that their sum equals one. As a result, signal events typically peak at values significantly below one, since the probability is distributed across all classes.

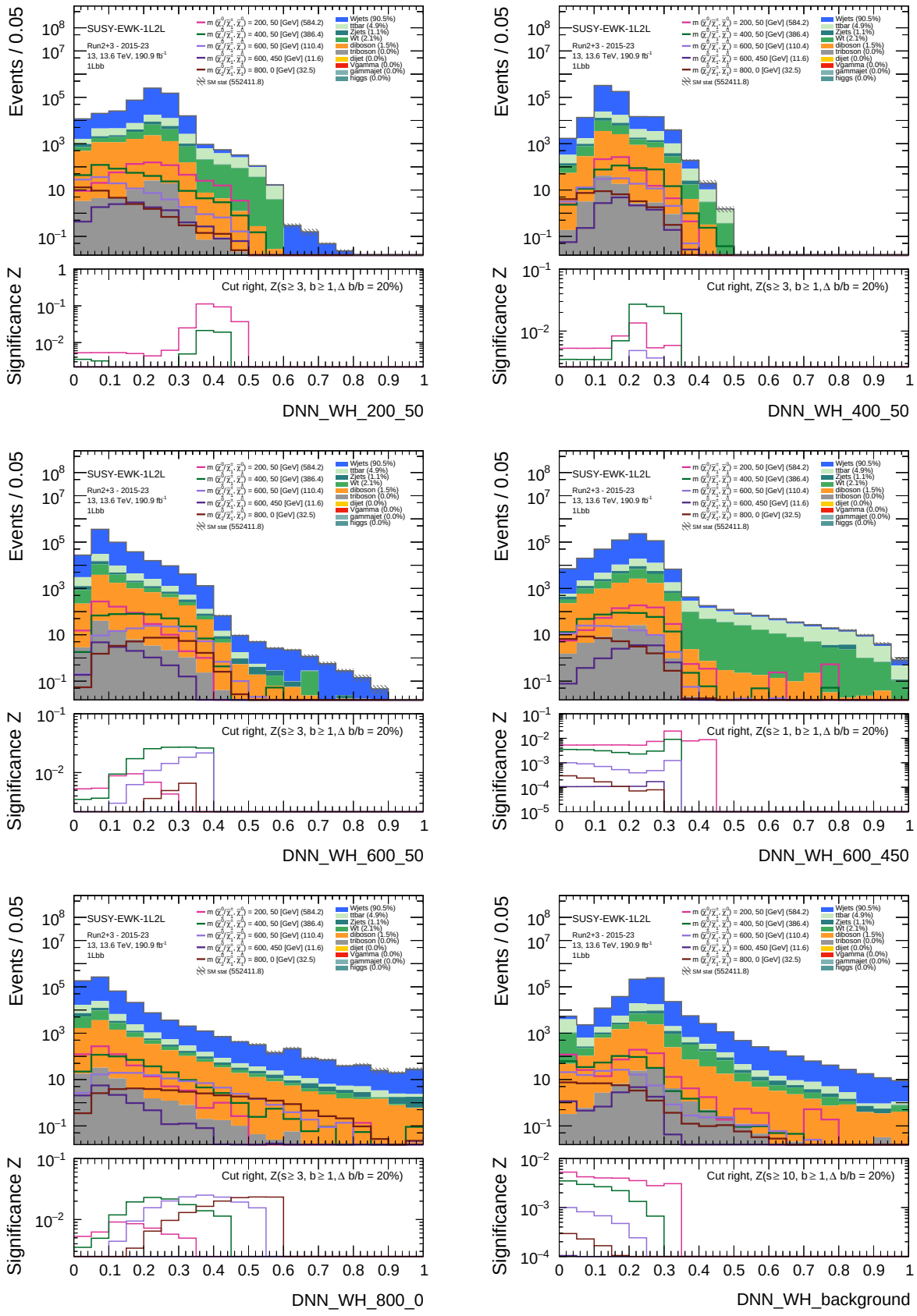

Figure 3.16: The top panel shows the output score distributions for the six DNN classes, corresponding to the benchmark mass hypotheses, within the 1Lbb region. The bottom panel show the behaviour of the significance.

Nevertheless, the plots demonstrate that the DNN retains a strong ability to distinguish signal from background. This is evident both from the increasing trend of the significance and from the fact that, for each class, the signal with the most right-shifted peak in the output score distribution corresponds to the signal with the appropriate mass splitting.

Subsequently, the distributions of the output score of the six different classes within the SRs defined in Table 3.4 were obtained. The most interesting results are shown as examples in Figures 3.17 and 3.18. The Z values obtained are significantly higher than those in the preselection region, demonstrating the effectiveness of the defined SRs.

In Figure 3.17, the plot on the left shows the DNN_WH_200_50 output score in the SRWh-SRLM-1L-boosted region. This output score is able to correctly distinguish the signal with mass hypothesis (200, 50) GeV from the background, as the trend of Z for the signal exhibits an increasing trend. Conversely, in the plot on the right this trend is decreasing, since in this case the distribution of the output score relative to the background is being studied.

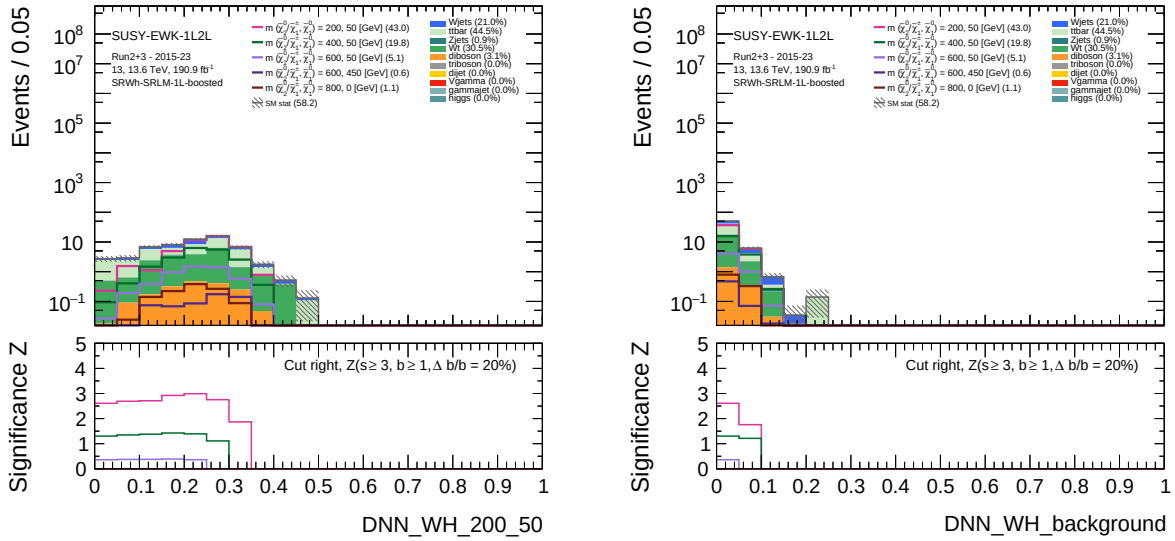

Figure 3.17: In the plot on the left the top panel displays the distributions of benchmark mass hypotheses for the variable DNN_WH_200_50 within the SR at low mass spitting. In the plot on the right it is shown the distribution of DNN_WH_background. The bottom panel show the behaviour of the significance.

In Figure 3.18, the distributions of the DNN_WH_400_50 and DNN_WH_600_50 output scores are shown in the medium mass SR and the distribution of the DNN_WH_800_0 output score is shown in the high mass SR. It can be observed that for each mass hypothesis of interest within the class of the DNN under consideration (for example, the (400, 50) GeV hypothesis for the output score DNN_WH_400_50), the behavior of Z shows an increasing trend.

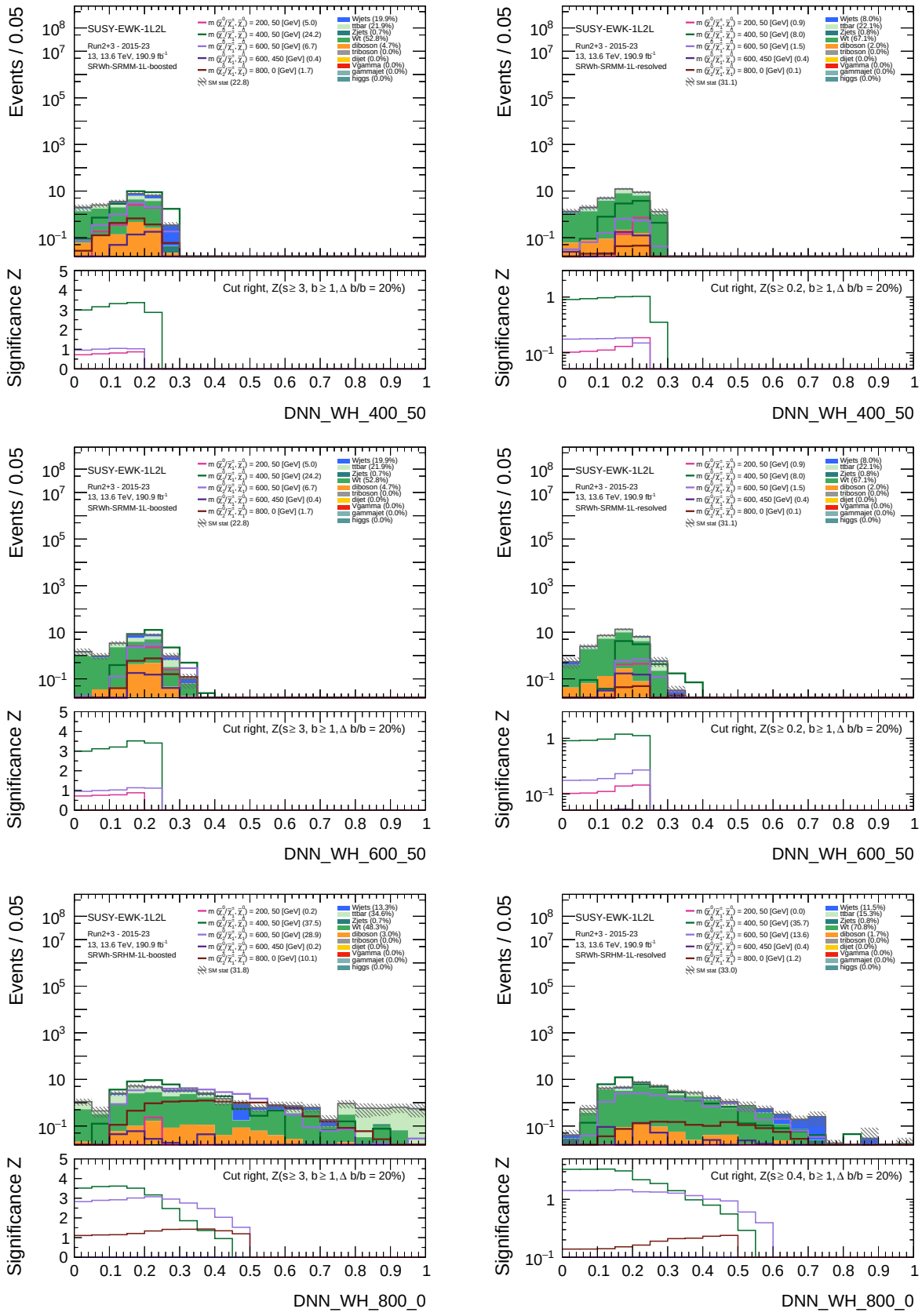

Figure 3.18: The top panel shows the distributions of benchmark mass hypotheses for the variables DNN_WH_400_50, DNN_WH_600_50 and DNN_WH_800_0 within the SRs with medium mass splitting. The bottom panel show the behaviour of the significance.

3.6.2 Variational Autoencoder

In addition to the DNN, a Variational Autoencoder (VAE) was employed in this analysis. The VAE is an unsupervised neural network model, meaning it is trained solely on unlabelled data and does not rely on signal identification as in the case of supervised classifiers like the DNN. It consists of two main components:

- an encoder, which maps an input data point x (e.g., a physics event described by a set of observables) into a latent distribution $q_\phi(z|x)$, typically a Gaussian parametrized by a mean $\mu(x)$ and standard deviation $\sigma(x)$;
- a decoder, which samples a vector z from the latent distribution and generates a reconstructed data point $\hat{x} = p_\theta(x|z)$.

The model is trained by minimizing the following loss function:

$$\mathcal{L}(x) = E_{q_\phi(z|x)}[\log p_\theta(x|z)] - D_{\mathrm{KL}}(q_\phi(z|x) \parallel p(z)), \tag{3.13}$$

where D_{KL} denotes the Kullback-Leibler divergence between the learned latent distribution $q_\phi(z|x)$ and a chosen prior $p(z)$, typically a standard normal distribution.

In practice, the reconstruction term is approximated by the Mean Squared Error (MSE) between the input x and its reconstruction $\hat{x}$, defined as

$$\mathrm{MSE} = \|x - \hat{x}\|^2. \tag{3.14}$$

The KL divergence term is computed analytically and given by

$$\mathrm{Loss}_{\mathrm{KL}} = \frac{1}{2} \sum_{i=1}^{d} \left(\mu_i^2 + \sigma_i^2 - \log \sigma_i^2 - 1 \right), \tag{3.15}$$

where μ_i and σ_i are the parameters of the approximate posterior for the i-th latent dimension, and d is the dimension of the latent space. The total VAE loss is thus VAE Loss = MSE + $\mathrm{Loss}_{\mathrm{KL}}$.

Once trained, the network is applied to a mixed dataset of signal and background events to identify potential anomalies. Events with a high total VAE loss are considered more likely to be signal-like, as they deviate from the learned background distribution and are poorly reconstructed by the network.

The VAE offers both advantages and limitations compared to the DNN. On one hand, it is more general and flexible, making it suitable for identifying anomalies or unknown structures in the data. On the other hand, due to its unsupervised nature, it may be less effective in achieving a sharp separation between signal and background compared to a supervised classifier.

In this analysis, the VAE was applied to distinguish the signal benchmarks with masses $m(\tilde{\chi}_1^\pm/\tilde{\chi}_2^0, \tilde{\chi}_1^0) = (200, 50)$ GeV and $(800, 0)$ GeV from the background in the region of preselection and in those defined in Table 3.4. Figures 3.19 and 3.20 show the VAE Loss distributions in the preselection region as well as in each of the six SRs previously defined.

Focusing on Figure 3.19, it can be observed that the VAE achieves good separation for the high-mass splitting signals, where the statistical significance Z shows a monotonically increasing trend; whereas its performance is less effective for the low-mass splitting candidates, as evidenced by the variable behaviour of Z. For completeness, it should be noted that the trend of Z is interrupted for VAE Loss values greater than 54 due to the imposed condition $s \geq 3$. Additionally, the last bin shows a sharp increase in statistics because it includes VAE Loss values greater or equal than to 98.

With reference to Figure 3.20, suboptimal performance is observed in the LM and MM splitting regions, while it is significantly better in the HM splitting region. Under these conditions, in both the boosted and resolved configurations, the peak of the signal event distribution is shifted to the right compared to that of the background events, indicating a greater discriminating power of the VAE.

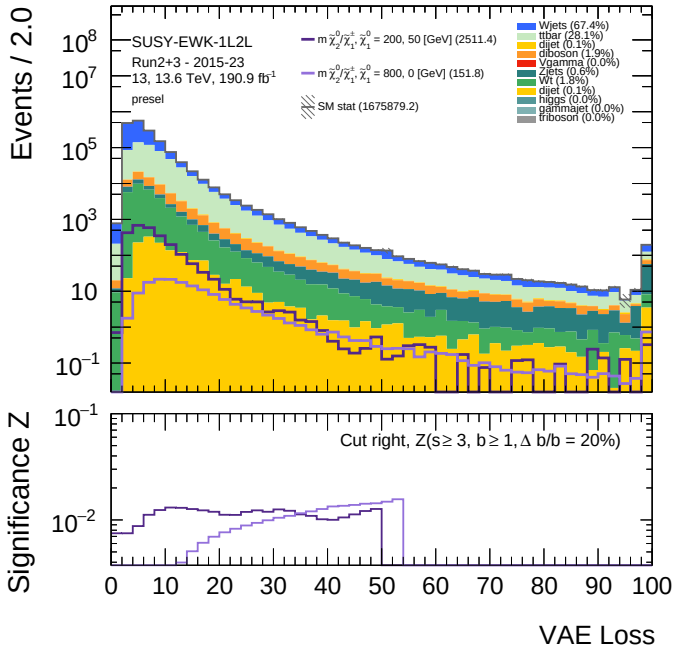

Figure 3.19: Signal and background distributions as a function of the VAE Loss in the preselection region (top panel), and cumulative significance (bottom panel).

A new SR, denoted as SRWh-SRHM-1L-boosted-cut, is defined by adding the condition VAE Loss ≥ 15 to the existing SRWh-SRHM-1L-boosted selection. The statistical significance Z is compared for the two regions using the first bin and the benchmark point (800, 0) GeV:

$$Z_{\text{SRWh-SRHM-1L-boosted}} = 2.31 \qquad Z_{\text{SRWh-SRHM-1L-boosted-cut}} = 2.65. \tag{3.16}$$

An improvement in the statistical significance is observed, indicating that the additional selection enhances the sensitivity to this signal.

Although the VAE is not well suited for defining new SRs or exploring unexplored signal mass hypotheses due to its unsupervised nature, its strong performance at large mass splitting makes it a valuable tool for validating benchmark points already examined in previous studies.

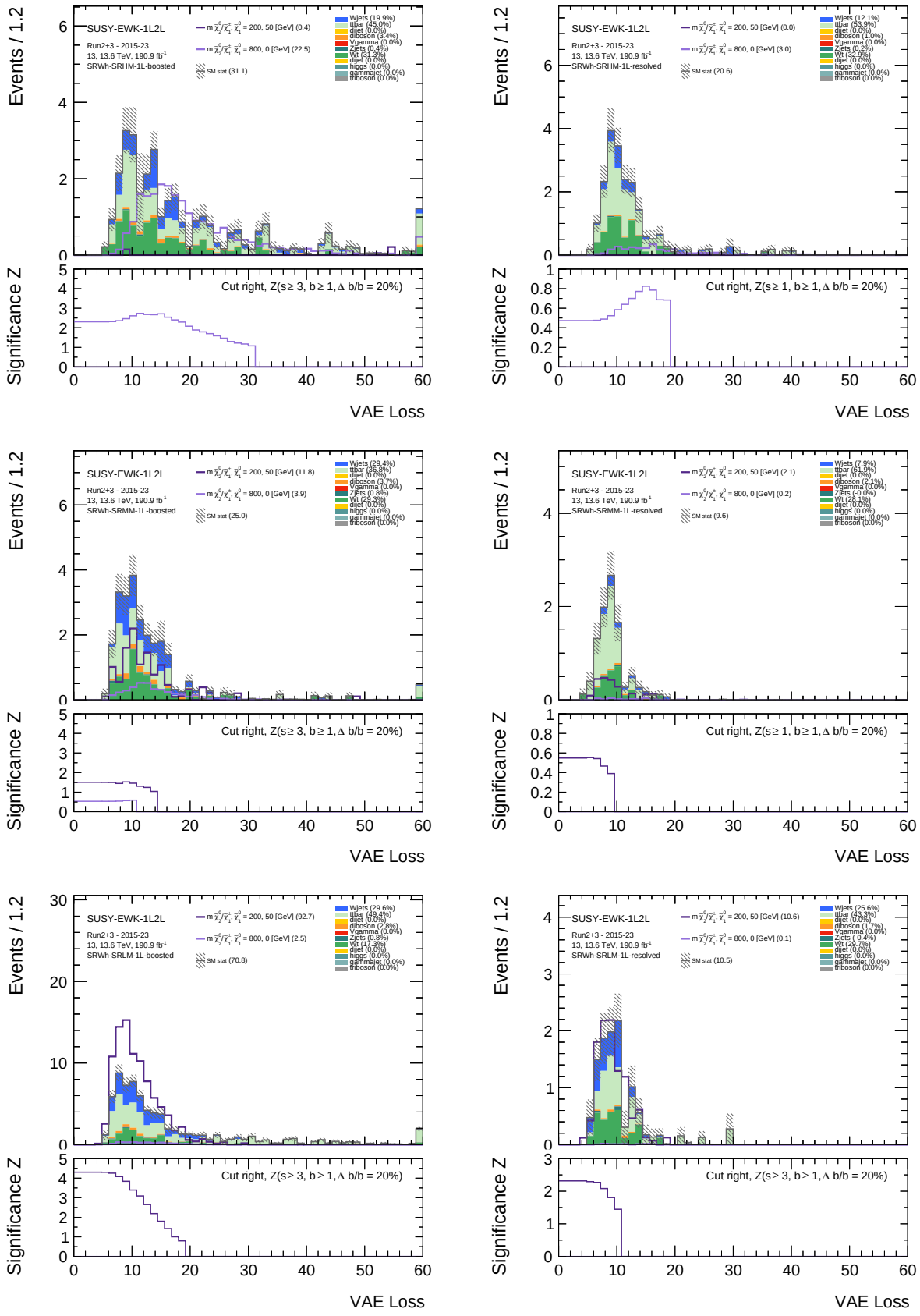

Figure 3.20: Signal and background distributions as a function of the VAE Loss in the six previously defined SRs (top panel), and cumulative significance (bottom panel).

3.7 Optimization of the Statistical Significance

By reapplying the C&C method, it was possible to further enhance the statistical significance. In this case, the selection cuts were optimized to correspond to the maximum value of the significance Z. The analysis focused on the behaviour of Z in the cuts right plots for the variable m_{jj}, and therefore only a lower bound was applied to this variable. The applied cuts are summarized in Table 3.6.

SR	$\boldsymbol{m_{jj}}$ (GeV)
SRWh-SRLM-1L-resolved	> 0
SRWh-SRMM-1L-resolved	> 0
SRWh-SRHM-1L-resolved	> 0
SRWh-SRLM-1L-boosted	> 100
SRWh-SRMM-1L-boosted	> 80
SRWh-SRHM-1L-boosted	> 100

Table 3.6: Definition of the cuts applied on the invariant mass of the jets, m_{jj}, for the six SRs taken in consideration.

The same procedure was applied by defining specific cuts on the DNN output score variable, depending on the different mass hypotheses considered. These selections are summarized in Table 3.7, which shows the cuts applied in each of the previously defined SRs. While the cuts are identical across all mass hypotheses for most SRs, the SRWh-SRHM-1L-boosted region is treated differently. In this case, four distinct cuts were defined, each corresponding to a different range of mass splitting. Specifically, the first set of cuts applies to hypotheses with $0 \leq \Delta m < 300$ GeV, the second to $300 \leq \Delta m < 600$ GeV, the third to $600 \leq \Delta m < 900$ GeV, and the fourth to $\Delta m \geq 900$ GeV.

$\boldsymbol{\Delta m}$ (GeV)	**SR**	**DNN_200_50**	**DNN_400_50**	**DNN_600_50**	**DNN_800_0**
–	SRWh-SRLM-1L-resolved	–	–	–	–
–	SRWh-SRMM-1L-resolved	–	> 0.10	–	–
–	SRWh-SRHM-1L-resolved	–	> 0.20	> 0.20	–
–	SRWh-SRLM-1L-boosted	> 0.20	–	–	–
–	SRWh-SRMM-1L-boosted	–	> 0.10	> 0.15	–
$\in [0, 300)$	SRWh-SRHM-1L-boosted	> 0.05	> 0.15	> 0.20	–
$\in [300, 600)$	SRWh-SRHM-1L-boosted	–	> 0.05	> 0.20	–
$\in [600, 900)$	SRWh-SRHM-1L-boosted	–	–	> 0.25	> 0.25
≥ 900	SRWh-SRHM-1L-boosted	–	–	–	> 0.30

Table 3.7: Definition of the cuts used to increase Z in the six SRs defined in Table 3.4. For SRHM-boosted, different cuts were applied depending on the mass splitting of the considered mass hypothesis.

3.8 Results

To estimate the significance value for each mass hypothesis obtained from the six regions defined in Table 3.4, the quadrature sum of the significances in each of the six SRs was calculated. The significance of each SR is estimated from the first bin of the significance cumulated from the right. Where it was not possible to compute Z using Equation 3.1 due to the requirement $s > 3$, we instead applied Equation 3.2. The significance values obtained are shown in Figure 3.21.

The same procedure was repeated considering both the cuts applied on the variable m_{jj}, and the cuts on the DNN output scores. The resulting significance values are presented respectively in Figures 3.22 and 3.23. As expected, the significance improved with both methods; however, the optimal result was achieved using the cuts based on the DNN output. This highlights the superiority of the DNN approach compared to the traditional C&C method, as expected from the fact that the DNN, and especially a multiclass DNN, is able to capture and exploit correlations among the input features.

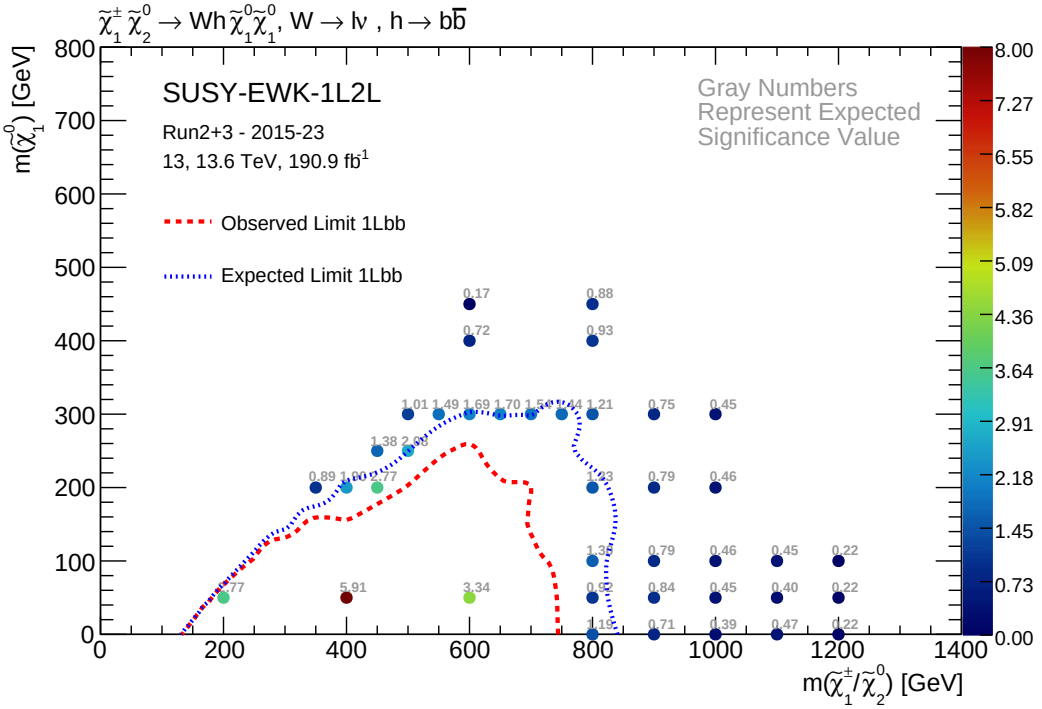

Figure 3.21: Z values for each point obtained from the six SRs defined in Table 3.4.

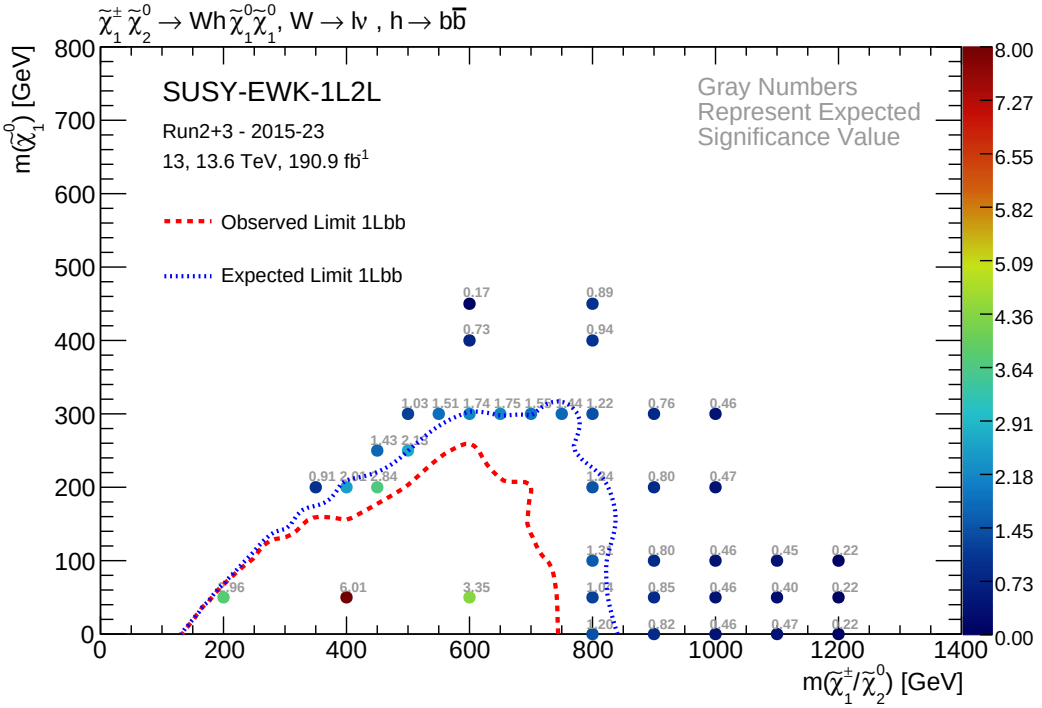

Figure 3.22: Z values for each point obtained applying the cuts defined in Table 3.6.

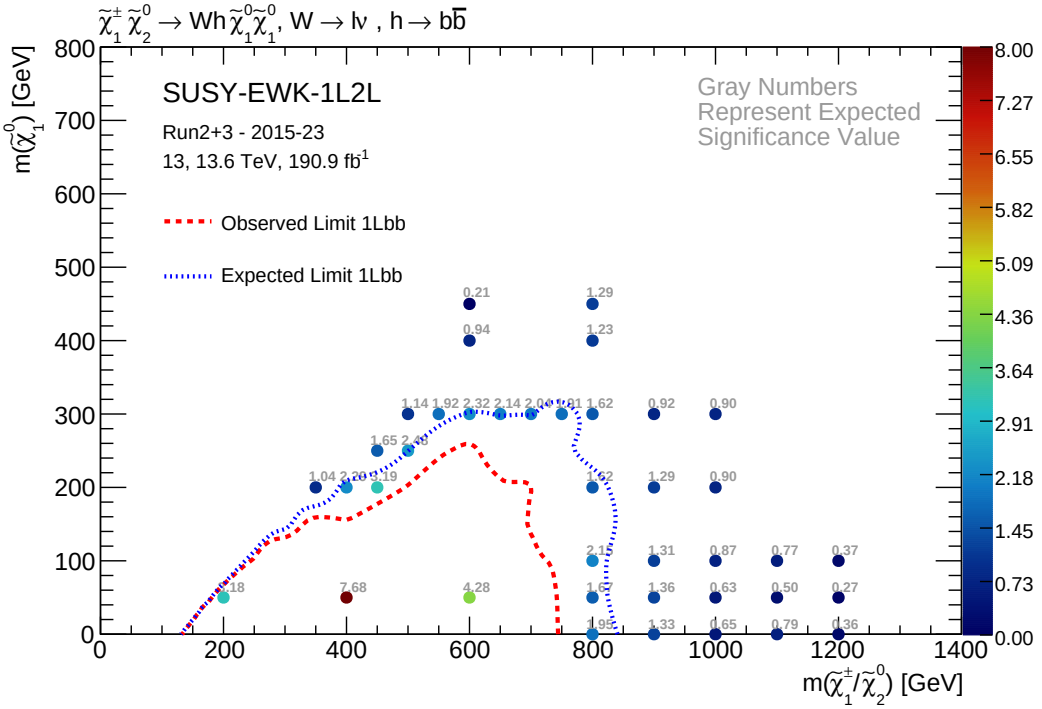

Figure 3.23: Z values associated with each point obtained by applying the cuts defined in Table 3.7.

Conclusion

This work focuses on the SUSY electroweakino pair production process: $pp \to \tilde{\chi}_1^{\pm}\tilde{\chi}_2^0$, where the chargino decays via $\tilde{\chi}_1^{\pm} \to \tilde{\chi}_1^0 W$, and the second-lightest neutralino via $\tilde{\chi}_2^0 \to \tilde{\chi}_1^0 h$. Unlike previous analyses of this process [23], the current study does not assume a fixed decay mode for the W boson and the h boson, but instead considers the BRs of the SM for these bosons. As a result, the analysis focuses on final states with one or two charged leptons. Signal and background events are simulated and reconstructed with the ATLAS detector, based on the integrated luminosity collected during Run 2 and partially during Run 3 (2022–2023). This study is part of a broader analysis effort that will also considers other decay modes for the SUSY particle and will also include the data collected during 2024 to further improve the sensitivity to electroweakino production.

By studying the single charged lepton channel, six SRs were defined through the application of a C&C method. In this channel, the performance of a VAE was considered, showing good performance in the SRs for signals with a large mass splitting, e.g. $\Delta m = 800$ GeV, that look different than the SM backgrounds. Due to its unsupervised nature, the VAE considered was not optimized to maximize significance for specific mass hypotheses, nor for testing signal mass hypotheses with low cross sections that would require a supervised approach. However, the VAE could be used to optimise the signal separation of mass hypotheses already excluded in previous results.

A further optimization step was carried out, relying on a cut-based selection or a DNN strategy, improving the statistical significance of the previously defined SRs. In particular, by applying optimized cuts on the DNN output score, the following significance values were obtained for two of the benchmark mass hypotheses considered, $m(\tilde{\chi}_1^{\pm}/\tilde{\chi}_2^0, \tilde{\chi}_1^0) = (500, 250)$ GeV and $(800, 0)$ GeV: $Z_{(500,250)} = 2.48$ and $Z_{(800,0)} = 1.79$. The results show a superior effectiveness of the DNN-based strategy with respect to a cut-based selection on the transverse dijet mass to further optimize the SR selection in terms of the statistical significance.

In addition, the dilepton channel was explored for the first time. Since this channel is rarer than the single-lepton one, it exhibited very low values of statistical significance, as expected. A more detailed investigation is left to future studies.

The analysis presented here improves the expected sensitivity with respect to the the previous results of the same process in the single-lepton channel. Given the promising capability of the DNN to distinguish between a variety of signal hypothesis and the SM background, such analysis technique can be adopted to guide the optimization of the future analysis targeting this model and achieve even larger sensitivity for electroweakinos.

Bibliography

[1] M.K. Gaillard, P.D. Grannis, and F.J. Sciulli, *The Standard Model of Particle Physics,* Rev. Mod. Phys. 71 (1999), S96–S111. https://arxiv.org/abs/hep-ph/9812285v1.

[2] CMS Collaboration, *High-precision measurement of the W Boson Mass with the CMS experiment at the LHC*, (2024). https://doi.org/10.48550/arXiv.2412.13872.

[3] LHC Collaboration, *Measurement of the Z-boson mass*, (2025). https://doi.org/10.48550/arXiv.2505.15582.

[4] J. Ellis, M.K. Gaillard, and D.V. Nanopoulos, *An updated historical profile of the Higgs boson*, (2015). https://doi.org/10.1142/9789814733519_0014.

[5] ATLAS Collaboration, *Combined measurement of the Higgs boson mass from the $h \to \gamma\gamma$ and $h \to ZZ^* \to 4\ell$ decay channels with the ATLAS detector using $\sqrt{s} = 7, 8$ and 13 TeV pp collision data*, Phys. Rev. Lett. 131 (2023) 251802. https://doi.org/10.1103/PhysRevLett.131.251802.

[6] J.L. Feng, *Naturalness and the status of supersymmetry*, (2013). https://arxiv.org/abs/1302.6587.

[7] D.J. Griffiths, *Elementary particles*, Weinheim, Chichester: Wiley-VCH; John Wiley distributor (2008).

[8] C. Csaki, *The minimal Supersymmetric Standard Model (MSSM)*, Mod. Phys. Lett. A11:599 (1996). https://arxiv.org/abs/hep-ph/9606414.

[9] T.S. van Albada et al., *Distribution of dark matter in the spiral galaxy NGC 3198, ADS*, Astrophysical Journal, Vol. 295, p. 305-313 (1985). https://ui.adsabs.harvard.edu/abs/1985ApJ...295..305V/abstract.

[10] W. de Boer, *Grand unified theories and supersymmetry in particle physics and cosmology*, Prog. Part. Nucl. Phys. 33:201-302 (1994). https://arxiv.org/abs/hep-ph/9402266.

[11] ATLAS Collaboration, *Luminosity determination in pp collisions at $\sqrt{s} = 13$ TeV using the ATLAS Detector at the LHC*, Eur. Phys. J. C 83 (2023) 982. https://doi.org/10.1140/epjc/s10052-023-11747-w.

[12] ATLAS Collaboration, *The ATLAS Experiment at the CERN Large Hadron Collider*, JINST 3 (2008) S08003. https://iopscience.iop.org/article/10.1088/1748-0221/3/08/S08003.

[13] CMS Collaboration, *The CMS experiment at the CERN LHC*, JINST 3 (2008) S08004. https://iopscience.iop.org/article/10.1088/1748-0221/3/08/S08004.

[14] ALICE Collaboration, *The ALICE experiment at the CERN LHC*, JINST 3 (2008) S08002. https://iopscience.iop.org/article/10.1088/1748-0221/3/08/S08002.

[15] LHCb Collaboration, *The LHCb Detector at the LHC*, JINST 3 (2008) S08005. https://iopscience.iop.org/article/10.1088/1748-0221/3/08/S08005.

[16] ATLAS Collaboration, *Performance of the ATLAS Trigger system in 2015*, Eur. Phys. J. C 77 (2017) 317. https://doi.org/10.1140/epjc/s10052-017-4852-3.

[17] ATLAS Collaboration, Aad G., Abbott B. et al., *Electron and photon efficiencies in LHC Run 2 with the ATLAS experiment*, J. High Energ. Phys. 2024, 162 (2024). https://doi.org/10.1007/JHEP05(2024)162.

[18] Aad G., Abbott B., Abeling K. et al., *Studies of the muon momentum calibration and performance of the ATLAS detector with pp collisions at* $\sqrt{s} = 13$ *TeV*, Eur. Phys. J. C 83, 686 (2023). https://doi.org/10.1140/epjc/s10052-023-11584-x.

[19] P. Ilten et al., *Modeling Hadronization using machine learning*, (2022). https://doi.org/10.48550/arXiv.2203.04983.

[20] Aad G., Abbott B., Abbott D.C. et al., *ATLAS flavour-tagging algorithms for the LHC Run 2 pp collision dataset*, Eur. Phys. J. C 83, 681 (2023). https://doi.org/10.1140/epjc/s10052-023-11699-1.

[21] ATLAS Collaboration, *Transforming jet flavour tagging at ATLAS*, CERN-EP-2025-103. https://doi.org/10.48550/arXiv.2505.19689.

[22] ATLAS Collaboration, *The performance of missing transverse momentum reconstruction and its significance with the ATLAS detector using 140* fb^{-1} *of* $\sqrt{s} = 13$ *TeV pp collisions*, Eur. Phys. J. C 85 (2025) 606. https://doi.org/10.1140/epjc/s10052-025-14062-8.

[23] ATLAS Collaboration, *Search for direct production of electroweakinos in final states with one lepton, missing transverse momentum and a Higgs boson decaying into two b-jets in pp collisions at* $\sqrt{s} = 13$ *TeV with the ATLAS Detector*, Eur. Phys. J. C 80 (2020) 691. https://doi.org/10.1140/epjc/s10052-020-8050-3.

[24] CMS Collaboration, *Search for chargino-neutralino production in events with Higgs and W bosons using 137* fb^{-1} *of proton-proton collisions at* $\sqrt{s} = 13$ *TeV*, JHEP 10 (2021) 045. https://doi.org/10.1007/JHEP10(2021)045.

[25] LHC Higgs Cross Section Working Group., Denner, A., Heinemeyer, S. et al., *Standard model Higgs-boson branching ratios with uncertainties*, Eur. Phys. J. C 71, 1753 (2011). https://doi.org/10.1140/epjc/s10052-011-1753-8.

[26] CMS Collaboration, *Precision measurement of the W boson decay branching fractions in proton-proton collisions at* $\sqrt{s} = 13$ *TeV*, Phys. Rev. D 105 (2022) 072008. https://doi.org/10.1103/PhysRevD.105.072008.

[27] ATLAS Collaboration et al., *Precision electroweak measurements on the Z resonance*, Phys. Rept. 427:257-454 (2006). https://arxiv.org/abs/hep-ex/0509008.

[28] ATLAS Collaboration, *Formulae for estimating significance, CERN Document Server*, CERN (2020). https://cds.cern.ch/record/2736148.

[29] E. Ballabene, *Search for electroweak production of supersymmetric particles in compressed mass spectra with the ATLAS detector at the LHC*, CERN-THESIS-2022-161. https://doi.org/10.48550/arXiv.2211.11642.

[30] F. Chollet et al., *Keras*, (2015). https://keras.io/.
[31] M. Abadi et al., *TensorFlow: A System for Large-Scale Machine Learning*, (2015). https://www.tensorflow.org/.
[32] D.P. Kingma and J. Ba, *A method for stochastic optimization*, (2014). https://arxiv.org/abs/1412.6980.